

Chapter 1

Bulk and surface properties of SmB_6

Priscila F. S. Rosa^{a,*} and Zachary Fisk^b

^a*Los Alamos National Laboratory, Los Alamos NM 87545, U.S.A.*

^b*University of California at Irvine, Irvine CA, U.S.A.*

*E-mail address: pfsrosa@lanl.gov

Abstract

Samarium hexaboride crystallizes in a simple cubic structure (space group #221, $Pm\bar{3}m$), but its properties are far from being straightforward. Initially classified as a Kondo insulator born out of its intriguing intermediate valence ground state, SmB_6 has been recently predicted to be a strongly correlated topological insulator. The subsequent experimental discovery of surface states has revived the interest in SmB_6 , and our purpose here is to review the extensive and in many aspects perplexing experimental record of this material. We will discuss both surface and bulk properties of SmB_6 with an emphasis on the role of crystal growth and sample preparation. We will also highlight the remaining mysteries and open questions in the field.

Rare-Earth Borides

Dmytro S. Inosov (ed.)

Copyright © 2020 by Jenny Stanford Publishing Pte. Ltd.

www.jennystanford.com

2 | Chapter 1 Bulk and surface properties of SmB₆

1.1 Introduction

First synthesized in polycrystalline form in 1932, SmB₆ started to be more heavily studied only in the 1970s owing to the successful growth of single crystals, the prospect of its use in thermoionic emission applications, and its intriguing mixed valence (Sm^{2.6+}), which gives rise to a Kondo-insulating ground state. The properties of SmB₆ have been investigated by a wide variety of experimental techniques and have been reported in more than 800 scientific articles, with about half of them being published just in the past decade. This flourish of research was motivated, to a great extent, by theoretical predictions invoking topological concepts recently extended to condensed-matter physics. SmB₆ remains a puzzling material, and here we take the challenge of reviewing our current knowledge of its bulk and surface properties.

This book chapter is organized as follows. First, we will discuss structural aspects and crystal growth methods typically used to synthesize single crystals of SmB₆. We will then present a very brief summary of proposed theoretical models. The third and fourth sections will review surface and bulk properties of SmB₆, respectively.

1.2 Crystal growth and structural properties

An important message of this chapter is that the physical properties of SmB₆ are sensitive to growth conditions. It will become clear in the next sections that advances in materials characterization have made the investigation of single crystals the current accepted norm, but we note that SmB₆ was first synthesized in polycrystalline form via borothermal reduction [1]. Typically, a homogeneous mixture of samarium oxide (Sm₂O₃) and boron powder is pressed into a pellet and heated by induction to temperatures from 1500 to 1800 °C in vacuum or in a hydrogen atmosphere [2].

For the growth of single-crystalline SmB₆, molten flux and floating-zone methods are the typical methods of choice. The molten-flux technique often allows the use of a suitable low-melting-point element that acts as a solvent out of which crystals can be grown at much lower temperatures than the melting point

of the compound [3–5]. This is particularly true here for SmB_6 , and aluminum is the flux of choice. Though the solubility of hexaborides in molten Al is quite low in general, melts with typical concentration of the hexaboride of order 10^{-3} molar make the growth of millimeter-sized single crystals possible. The synthesis is performed in alumina tube furnaces at temperatures from 1500 to 1150 °C in a protective atmosphere of ultra-high-purity argon, which flows at a slow rate. Usually, 50 ml alumina crucibles hold the melts, and chemical etching with NaOH solution is used to remove the Al at room temperature. A more benign leaching can be accomplished by growing from an Al-Ga melt, which can be leached using H_2O . Independent of the etching procedure, the etchant does not attack the hexaboride; however, larger crystals often enclose Al lamellae which cannot be removed by etching. This is the main disadvantage of synthesizing SmB_6 out of flux. As we will discuss below, x-ray computed tomography experiments on flux-grown crystals reveal the presence of co-crystallized, epitaxial aluminum. Nevertheless, aluminum inclusions can be mechanically removed by polishing.

The traditional optical-image floating zone growth technique is based on the directional solidification of a crystal from a liquid floating zone heated by bulb lamps and parabolic mirrors [6]. The elimination of an alumina crucible and of the aluminum flux prevents some of the issues with the flux technique; however, crystals grown by the floating zone method require much higher temperatures ($T > 2000$ °C), which lead to composition variations. Powder x-ray diffraction in consecutive cuts of a floating-zone grown crystal reveals a systematic change in lattice parameters [7]. Precisely identifying the origin of the composition change (e.g. Sm/B vacancies, crystallographic defects, etc.) is challenging and remains a major open question in the field.

The simple CsCl-type arrangement of metal atoms and B_6 octahedra found in the rare-earth and alkaline-earth hexaborides was known from the early x-ray studies [8,9]. The electronic closed-shell configuration for a B_6 octahedron in this structure was determined later by molecular cluster calculations [10]. Twenty electrons were found to be required for the closed-shell configuration of an octahedron. This finding suggested that divalent metals forming

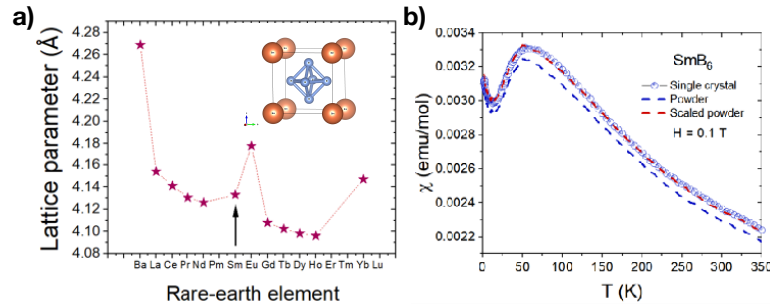
4 Chapter 1 Bulk and surface properties of SmB_6 

Figure 1.1 (a) Lattice parameters of the cubic hexaborides RB_6 (R is a rare-earth element) at room temperature. Inset shows the cubic unit cell. (b) Temperature dependent magnetic susceptibility measured on an Al-flux grown single crystal as well as its powder. The scaling factor is 1.05 to account for a small loss of powder mass.

hexaborides should be semiconducting, whereas trivalent ones should be metallic. Subsequent de Haas–van Alphen studies of metallic LaB_6 were consistent with this picture, finding a Fermi surface containing one electron per formula unit [11, 12]. Measurements of the ordinary Hall coefficient in PrB_6 and NdB_6 also found one electron per formula unit [13].

SmB_6 , however, is neither divalent nor trivalent. The intermediate valence character of SmB_6 is already seen in the hexaboride lattice parameter variation across the rare-earth sequence shown in Fig. 1.1 (a). The majority of rare-earth hexaborides is trivalent, whereas EuB_6 and YbB_6 are strictly divalent. Hexaborides with Er, Tm, and Lu do not form, possibly because their metallic radii are too small for the structure to be stable. Further evidence for the mixed valence comes from magnetic susceptibility measurements, shown in Fig. 1.1 (b). At high temperatures, the magnetic susceptibility of SmB_6 falls between the values expected for Sm^{2+} (Van Vleck) and for Sm^{3+} ($J = 5/2$ moment). Below about 60 K, the magnetic susceptibility decreases with decreasing temperature, in agreement with the opening of a gap. At temperatures below about 14 K, a Curie-like tail is observed. This tail is sample dependent, and measurements on a powdered single crystal indicate that it is a bulk effect [Fig. 1.1 (b)].

1.3 Theoretical remarks

Studies of other intermediate valence rare-earth compounds with features similar to those seen in SmB_6 led to the suggestion of their classification as Kondo insulators, a group of semiconducting compounds containing f -elements which do not order magnetically [14]. As a result, an isostructural semiconducting compound forming with non- f elements has the integral valence of one of the f -configurations of the Kondo insulator. SmB_6 is seen as a prototypical Kondo insulator, the non- f semiconducting counterparts being the alkaline-earth hexaborides. Though Kondo physics usually seems quite distinct from that of intermediate valence, in the case of SmB_6 it was found that dilute Sm impurities in divalent SrB_6 showed a Kondo scale of 3 K, whereas dilute Sm impurities in trivalent LaB_6 appeared to be divalent, $4f^6$, with no Kondo behavior. This appears consistent with lattice parameter alloys studies of $\text{SmB}_6/\text{LaB}_6$ and $\text{SmB}_6/\text{YbB}_6$ in which Sm appears to go in as divalent and trivalent ions, respectively [15]. Perhaps the most accepted picture that emerged for this class of small gap semiconducting materials is that the narrow gap arises from hybridization between the $4f$ electrons and d conduction bands at the Fermi level [16, 17]. Other early scenarios include Wigner crystallization in the Kondo lattice [18] and exciton-polaron models of charge fluctuations [19]. In the former, carrier localization occurs owing to correlations. In the latter, an electronic instability leads to a mixed-valence state hosting a soft electronic exciton with mixed $4f$ and $5d$ wave functions. A more recent scenario argues for a mixed-valence state originated from an unrecognized dynamical bonding effect, i.e., the coexistence of two Sm-B bonding modes corresponding to two different oxidation states driven by the motion of boron [20, 21].

In 2010, SmB_6 was proposed to be the first topological Kondo insulator, i.e., a material that hosts a topologically protected surface state surrounding an insulating bulk driven by hybridization between Sm f electrons and conduction d electrons [22]. Band structure calculations indicate that the parity of the hybridized bands is inverted at three symmetry-equivalent X-points in the cubic Brillouin zone. The resulting topological invariant therefore

6 | Chapter 1 Bulk and surface properties of SmB_6

predicts a non-trivial topological insulating state [23–25]. Further, motivated by the unusual bulk properties we discuss below, more recent theories involve ingredients such as neutral Fermi surfaces, spin excitons, fractionalized quasiparticles and disorder [26–37]. Our goal here is not to present a detailed overview of the numerous theories, but instead to present the ensemble of experimental data against which these theories need to be checked. For theoretical reviews, we refer the reader to [38–40].

1.4 Surface properties

1.4.1 *dc electrical conductivity*

Figure 1.2 displays a summary of representative dc electrical resistivity (panel a) and resistance (panel b) data of SmB_6 [41–45]. These measurements are typically performed in a four-point configuration using a low-frequency ac excitation and a lock-in amplifier for detection.

At high temperatures, the electrical resistance of SmB_6 increases with decreasing temperature, in agreement with an insulating response. At around 15 K, a broad feature usually emerges, which we will come to later. Finally, at temperatures below about 4 K,

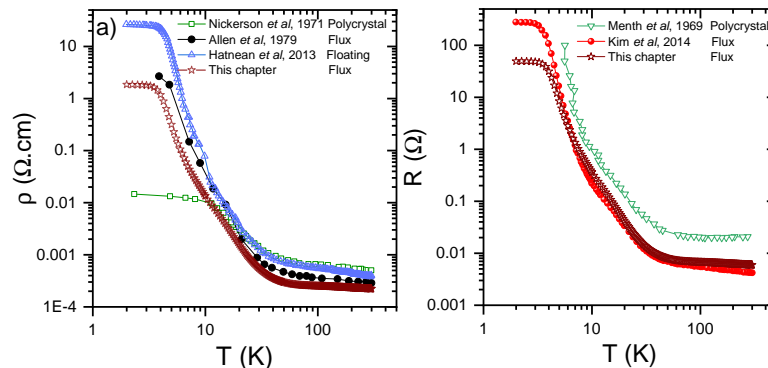


Figure 1.2 Compilation of temperature dependent (a) electrical resistivity and (b) electrical resistance obtained in SmB_6 samples grown by different methods. Reproduced from Menth *et al.* [41], Nickerson *et al.* [42], Allen *et al.* [43], Hatnean *et al.* [44] and Kim *et al.* [45].

the resistance saturates. This saturation was initially thought to be extrinsic and attributed to impurity conduction (e.g. holes from Sm vacancies); however, this plateau has been recently revisited due to the prediction of surface states.

In 2013, three independent groups reported clever ways of probing whether the resistance saturation is caused by surface states. The first way involves non-local measurements, as shown in Fig. 1.3 (a) [46]. Eight coplanar electrical contacts were attached on the (100) and $(\bar{1}00)$ surfaces of a polished flux-grown SmB_6 single crystal. The standard configuration used in previous measurements, R_{lat} , cannot distinguish surface and bulk conduction; however, measurements using contacts on opposite sides of the samples could. For instance, a vertical measurement, R_{vert} , is obtained by flowing current from one side of the sample to the opposite side and measuring the voltage drop on another pair of contacts also placed in opposite sides. Further, a hybrid measurement, R_{hybrid} , is obtained by flowing current on one side of the sample and measuring the voltage on the opposite side. Figure 1.3 (b) shows the experimental resistance, which is in agreement with the simulations taking into account the low-temperature surface-dominated conduction.

The second way of measuring the surface contribution with dc electrical resistance measurements is by polishing the sample to a well-defined wedge, as shown in the inset of Fig. 1.3 (c) [47]. By attaching several Hall voltage leads along the length of the sample, one can directly measure the thickness-dependent Hall response, as shown in the main panel of Fig. 1.3 (c). If dominated by the bulk, the Hall resistance should be inversely proportional to the thickness; however, if conduction occurs mainly on the surface, the Hall resistance should be independent of the thickness. In fact, the Hall resistance ratios between different thicknesses of a flux-grown SmB_6 sample become constant below about 4 K, as shown in Fig. 1.3 (d). The authors are also able to fit the experimental Hall data with a simple two-channel conduction model containing a temperature-independent surface channel and an activated bulk channel.

The third approach makes use of quasiparticle tunneling spectroscopy, which measures the bulk density of states [48]. The au-

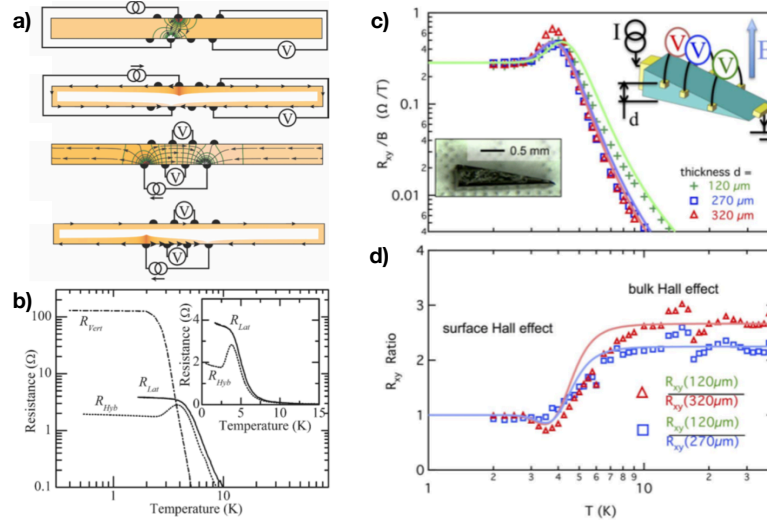
8 Chapter 1 Bulk and surface properties of SmB_6 

Figure 1.3 (a) Schematic diagram of the cross section of the sample and electrical contact configurations. Arrows indicate current direction, and lines indicate equipotentials. Reproduced from Wolgast *et al.* [46]. (b) Log-log plot of the experimentally determined electrical resistance vs. temperature in different configurations. Inset shows a linear plot of R_{lat} and R_{Hybrid} . Reproduced from Wolgast *et al.* [46]. (c) Temperature dependence of Hall resistance of SmB_6 at different thicknesses. Reproduced from Kim *et al.* [47]. (d) Hall resistance between different thicknesses. Reproduced from Kim *et al.* [47].

thors argue that, if the resistance saturation below 4 K were due to coherent transport from bulk in-gap states, the electronic structure would change and lead to a zero-bias peak. Their results, however, indicate that the bulk density of states is robust below 10 K, which is taken as evidence for a metallic surface state. Several resistivity studies followed the initial reports, including the use of ionic liquid gating, which supports the scenario of an insulating bulk at high temperatures and metallic surface states that dominate at low temperatures [49].

We note that all the measurements discussed so far were performed in flux-grown SmB_6 . To our knowledge, there are fewer similar experimental investigations on floating-zone samples, and the community would benefit from systematic dc electrical re-

sistivity measurements on these crystals. Here we mention two representative reports. In the first one, the authors performed R_{vert} and R_{hybrid} measurements on floating-zone samples and conclude that there is not only surface conduction at low temperatures, but also an additional residual bulk conduction possibly arising from a valence-fluctuation induced hopping from bulk in-gap states [50,51]. The second report performed a systematic resistivity measurement in different cuts of a floating zone grown crystal, and no significant plateau was observed below about 4 K, only a "knee" [52]. Systematic growths in the presence of carbon were then performed because carbon is a common impurity in boron. Remarkably, a thickness-independent plateau emerged in C-doped SmB_6 crystals. A sensible possibility suggested by the authors is that both topological and trivial surface states coexist as non-topological surface states may arise from chemical variations at the surface. For instance, as we will discuss below, the valence of Sm is observed to change to $3+$ at the surface (section 1.5.6), and the polar [001] surface is prone to polarity-driven surface states [53]. It is worth noting that a number of alternative theoretical proposals for the surface conductivity of SmB_6 have been put forward, including trivial surface states discussed above, impurity bands, phonon bound states due to magnetoelastic coupling, Wigner lattice, and Mott minimum conductivity. We therefore conclude that, though the community appears to agree that SmB_6 hosts surface states, the topological nature of these states remains unsettled.

In spite of the many possible scenarios for its origin, it is fair to state that surface conduction at low temperatures has been established via dc electrical resistivity. As a result, many more questions arise. Why is there a substantial variation in the low-temperature resistivity in Fig. 1.2? Can one probe the bulk resistance of SmB_6 without the influence of the surface states? What is the origin of the feature at 15 K? And finally, are these surface states topologically protected? The answer to the last question is still disputed, and the rest of this chapter will overview experimental results to help the reader reach a conclusion.

The answer to the first question likely lies on the experimental observations that the bulk-to-surface ratio influences the low-temperature crossover and that small subsurface cracks increase

10 Chapter 1 Bulk and surface properties of SmB_6

the surface conductivity [55]. As a result, the surface saturation will depend on how the sample was prepared — in particular, whether it is as-grown, roughly polished, or finely polished. As the surface quality improves (i.e. no cracks), the conductivity of the surface is reduced. This mechanism further explains the apparent high carrier density obtained in Hall measurements.

The evident consequence of the presence of two conduction channels, one of them with varying conductivity, is that one cannot use the typical inverted resistance ratio (i.e. $\text{IRR} = R_{2\text{K}}/R_{300\text{K}}$) as a good measure of the quality of the sample. This brings us to our next question: can one probe the bulk resistance of SmB_6

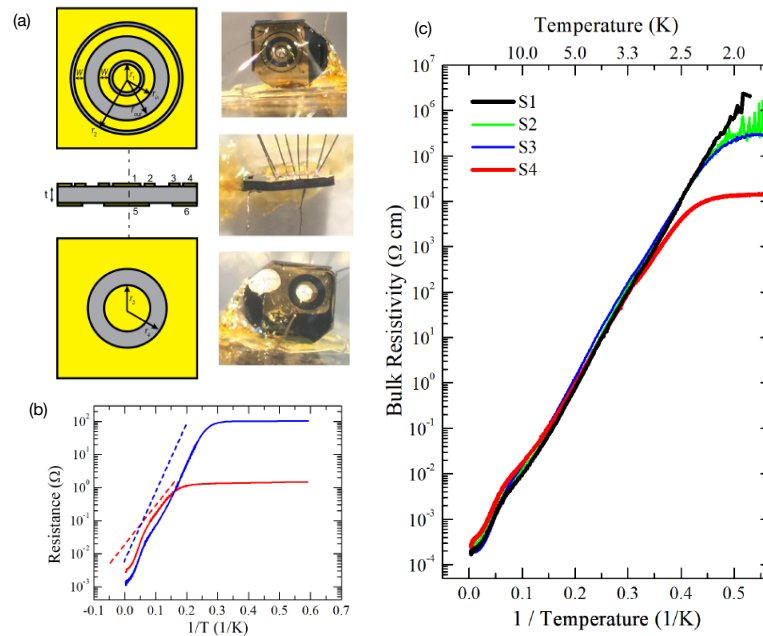


Figure 1.4 (a) Schematic diagram (left) and photograph (right) of the transport geometry used in double-Corbino measurements. (b) Electrical resistance as a function of reciprocal temperature for flux-grown SmB_6 crystals prepared for Corbino measurements (blue solid curve) and as-grown (red solid curve). (c) Bulk resistivity as a function of reciprocal temperature for a stoichiometric sample (S1) as well as samples grown with Sm vacancies (S2–S4). Figures Reproduced from Eo *et al.* [54].

without the influence of the surface states? The answer is yes, via Corbino-disk measurements [54]. The transport geometry for these measurements is shown in Fig. 1.4 (a). The flux-grown samples are first finely polished with a final step of aluminum oxide slurry of $0.3 \mu\text{m}$. The Corbino patterns are then fabricated on the sample via photolithography followed by e-beam evaporation of Ti/Au ($20 \text{ \AA}/1500 \text{ \AA}$). By preparing two Corbino disks on opposite surfaces, one can measure either the standard resistivity using just one of the Corbino disks or the so-called “inverted” resistivity by applying current on one Corbino and measuring voltage on the opposite one. Figure 1.4 (b) shows the difference in standard resistance between a sample prepared by the Corbino method (blue curve) and an as-grown sample measured by the usual four-probe configuration and no surface preparation (red curve). The significant difference further confirms that the magnitude of the resistance plateau is greatly sensitive to sample preparation. In addition, the extracted gap value also changes from one measurement to another. Figure 1.4 (c) shows the activated plot for the “inverted” resistivity measurements, which only probe the bulk of the sample. Remarkably, the bulk resistivity of flux-grown SmB_6 (S1) rises by 10 orders of magnitude on cooling from 300 to 2 K with no saturation at low temperatures. Samples grown off-stoichiometry with Sm vacancies do show saturation at low temperatures (S2–S4), indicating that the gap is robust against point defects and strikingly exponential over a range of temperature one would normally expect some deviations due to temperature dependent scattering rate. An open question is whether floating-zone samples exhibit a similar behavior.

The feature in dc electrical resistivity at about 15 K is not often discussed, but it is reproducible. A recent theoretical framework explains this feature by modeling SmB_6 as an intrinsic semiconductor with an accumulation length that diverges at cryogenic temperatures [56]. The self-consistent solution to Poisson’s equation taking into account surface charges leads to band bending in the valence and conduction bands as well as to a crossover at about 12 K to bulk-dominated conduction dominated by surface effects. The authors argue that band bending effects explains why the activated gap obtained from dc electrical resistance measurements is

12 | Chapter 1 Bulk and surface properties of SmB₆

smaller than the gap obtained from spectroscopy measurements: spectroscopic methods measure the gap near the surface, whereas transport probes the average gap over the bulk.

We end this section by mentioning dc electrical resistivity measurements on doped or irradiated SmB₆. Small amounts (~3%) of Gd in flux-grown SmB₆ were shown to destroy the surface conduction, whereas the resistance saturation remains intact for samples doped with nonmagnetic Y and Yb at the same concentration level [45]. This result was taken as evidence for topological surface states, which is destroyed by impurities that break time-reversal symmetry. Similarly, magnetic and nonmagnetic ion irradiation was used to damage the surface layers of flux-grown SmB₆ [57, 58]. The dc resistance results suggest that the surface state is not destroyed by ion irradiation, but instead it is reconstructed below the poorly conducting damaged layer, whether the damage was caused by a magnetic or a nonmagnetic ion. A recent doping study on floating-zone samples has investigated the dc electrical resistivity of SmB₆ doped with lanthanum, europium, ytterbium and strontium, revealing a complex response [59].

1.4.2 Tunneling spectroscopy and thermopower

The measurements presented in the previous section are an average over the whole surface of SmB₆, whereas scanning tunneling microscopy and spectroscopy measurements are able to probe the surface of SmB₆ on an atomic level. SmB₆, however, lacks a natural cleavage plane. As a result, various surface terminations are possible, and surface domains might emerge. Independent groups have performed density functional theory calculations of the surface formation energy for different surface terminations, as exemplified in Fig. 1.5 [60–62]. The lower energy pentaboride termination is argued to form disordered regions [62], whereas the 2 × 1 Sm termination was argued to be ordered and non-polar [63, 64], though this assignment has been questioned recently [65].

In fact, reports on flux-grown SmB₆ observed several distinct surface terminations on the same surface [61, 63, 64, 66, 67]. The crystals are typically cleaved *in situ*, and four main categories of 001 surface terminations have been observed: (i) Sm-terminated

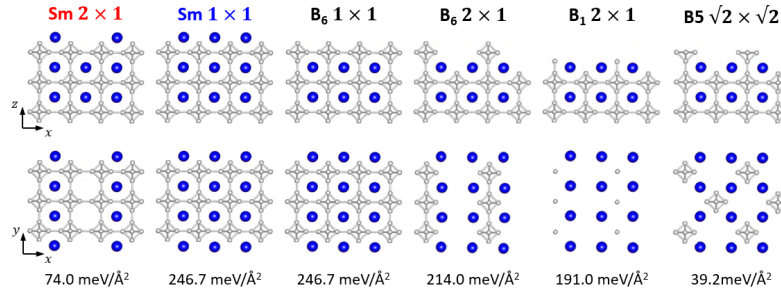


Figure 1.5 Surface formation energy of six different surface reconstructions in SmB_6 . Reproduced from Matt *et al.* [62].

surfaces; (ii) B-terminated surfaces; (iii) disordered reconstructed surfaces; and (iv) ordered reconstructed surfaces (e.g. 2×1), as shown in Fig. 1.6. Further, the temperature at which the crystals are cleaved appear to play a significant role in determining the surface termination [68]. At room temperature, Ruan *et al.* cleaved the samples through the B_6 octahedra, exposing a donut-shaped structure [66], whereas the cleavage planes appear between octahedra at lower temperatures [64]. Experimental reports on floating-zone samples, however, argued that only one topography is observed on a given surface, though the authors recognize they did not scan the entirety of the cleaved area [65]. For details on the surface termination assignment, we refer the reader to [69].

We recall that the bulk-truncated (001) surface of SmB_6 is polar, which could give rise to band bending, charge puddles, and the surface reconstructions mentioned above. Further, surface reconstructions could generate metallic surface layers, making the observation of a topologically non-trivial surface state challenging. In spite of the outstanding issues with surface termination, there are similarities between different reports we would like to highlight. First, a decrease in the dI/dV spectrum is observed in scanning tunneling microscopy experiments at about 10–20 meV at temperatures below ~ 35 K and attributed to the opening of the hybridization gap. The conductance, however, does not vanish at zero voltage, indicating a finite density of states at E_F , which is consistent with both an incomplete gap and an additional conductance channel at the surface. At lower temperatures, several

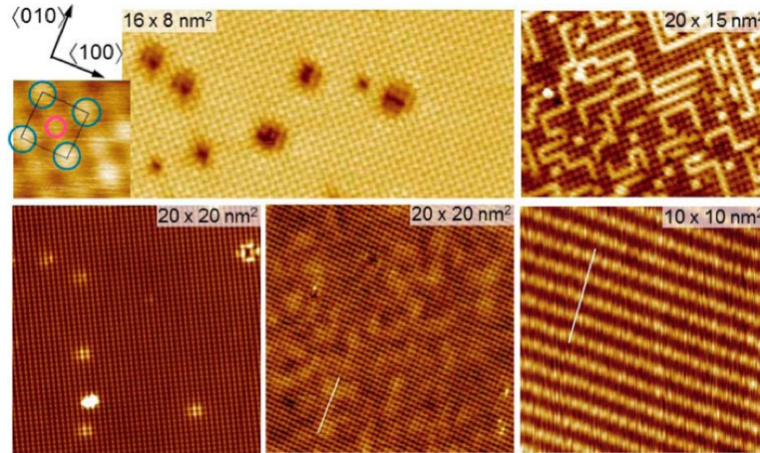
14 | Chapter 1 Bulk and surface properties of SmB_6 

Figure 1.6 Summary of representative topographies observed on cleaving a (001) SmB_6 surface. Reproduced from Rößler *et al.* [69]. The upper left and center topographies display Sm-terminated surfaces, whereas the bottom left and center topographies display B-terminated surfaces. The upper right topography shows a reconstructed disordered surface, whereas the bottom right topography shows a 2×1 reconstruction.

features emerge within the gap. In particular, a large sharp peak is observed at around -7 meV, even in reconstructed surfaces, though the origin of such feature is not agreed on. Jiao *et al.* argue that this feature contains not only a bulk contribution, but also a surface component below 7 K [67]. In Gd-doped SmB_6 , this -7 meV feature is destroyed at the impurity site with a healing length of approximately 1 nm in the vicinity of a defect. In addition, a magnetic tip is found to have significant effect on the local electronic structure. These findings are consistent with the expectation that the protected nature of a topological surface conducting state can be destroyed by time-reversal symmetry breaking [70]. Evidence for topologically non-trivial surface states is also presented by quasiparticle interference spectroscopy [63], which images the formation of linearly dispersing surface states with heavy effective masses (e.g. $m^* \sim 400m_e$ at the X point). Thermopower and Nernst effect measurements on the (110) plane of SmB_6 also indicate that the metallic surface state has a large effective mass [71].

Scanning tunneling spectroscopy measurements and analysis by Herrmann *et al.* [65], however, argue for a modification of the low-energy electronic structure at the surface, which would in turn give rise to topologically trivial surface conductivity due to the termination-dependent $4f$ -like intensity near the Fermi level.

Planar tunneling spectroscopy measurements are also sensitive to the surface, and a Pb-SmB₆ junction has been used to probe the spectroscopic properties of SmB₆ [72,73]. The differential conductance on both (100) and (110) surfaces display a peak at about -21 mV attributed to the bulk hybridization gap, in agreement with scanning tunneling spectroscopy measurements discussed above. Below about 15 K, the conductance increases, taken as an indication of a stronger surface state contribution, in agreement with the feature in dc resistivity discussed above. A V-shaped linear conductance is then observed at low bias arguably to the expected Dirac fermion density of states. This linearity, however, ends at about 4 mV and is attributed to inelastic tunneling via emission and absorption of bosonic excitations, i.e., spin excitons on the surface. The authors conclude, enlightened by theory, that the topological protection of the surface states is incomplete owing to their strong interaction with bulk spin excitons. As a result, low-energy protected surface states may only exist below 5–6 K when the interaction with spin excitons become negligible.

Finally, we note that no quantum oscillations were observed in dc resistance, planar tunneling spectroscopy or thermopower measurements described so far, though torque magnetometry measurements initially revealed oscillatory patterns as we will describe in the next section.

1.4.3 Quantum oscillations

The first report of quantum oscillations in SmB₆ used flux-grown crystals [74]. Li *et al.* used torque magnetometry to map the oscillation pattern as a function of temperature and angle, as exemplified in Fig 1.7 (a,b).

Three pockets were observed at $\alpha = 29$ T, $\beta = 286$ T and $\gamma = 385$ T with unexpectedly light effective masses of $m/m_e = 1.1, 0.8$ and 0.36 , respectively [Fig 1.7 (c,d)]. The presence of light quasi-

16 | Chapter 1 Bulk and surface properties of SmB_6

particles was argued theoretically to be due to a reduction of the Kondo effect on the surface associated with Kondo breakdown [29]. Both the effective masses and the angular dependence of the observed quantum oscillations, however, resemble that of aluminum, the flux used to prepare the single crystalline samples used in the experiment. Li *et al.* argued that the aluminum pellets used in the growth are polycrystalline and, as a result, could not generate the observed angular dependence. The authors therefore concluded that the measured Fermi surface cross sections scaled as the inverse cosine function of the magnetic field tilt angles, demonstrating the two-dimensional nature of the conducting (surface) states. The same group later showed that, though the angular dependence of the frequency of the β branch is fourfold symmetric, the angular dependence of the amplitude of the same branch is twofold sym-

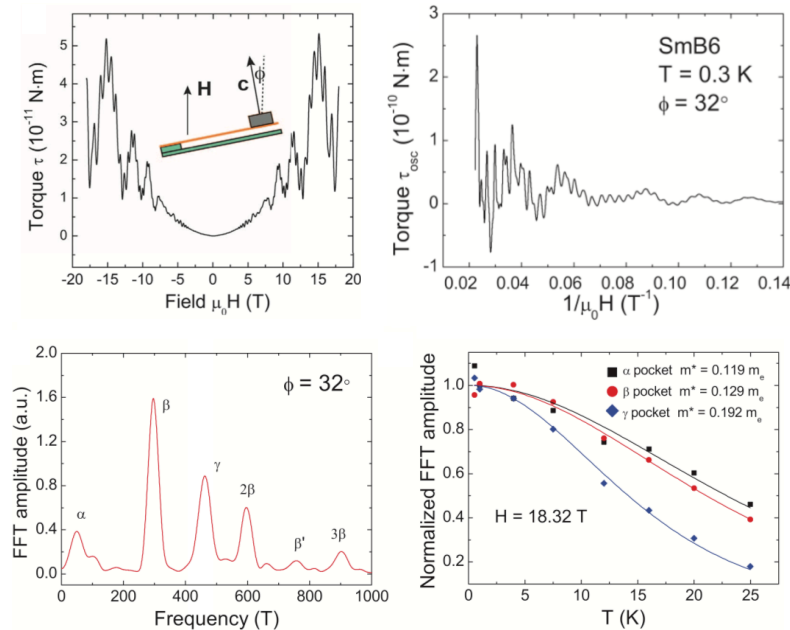


Figure 1.7 (a) Magnetic torque of flux-grown SmB_6 at 300 mK as a function of magnetic field. (b) Oscillatory torque as a function of reciprocal field. (c) Fast Fourier Transform (FFT) of the oscillatory torque. (d) Temperature dependence of the FFT amplitude. Reproduced from Li *et al.* [74].

metric. This result was taken as evidence of multiple light-mass surface states in SmB_6 [75].

A recent report on this subject has revisited the quantum oscillation patterns of flux-grown SmB_6 [76]. Thomas *et al.* were only able to observe quantum oscillations in about 50% of the samples, and these samples tended to have larger thickness. As mentioned in the section 1.2, the main disadvantage of the flux technique in this case is that flux could become an inclusion. As a result, a thickness-dependent study was performed on the thicker samples displaying quantum oscillations. Care was taken to polish only one side of the sample to maintain any quantum oscillations coming from the other surfaces intact. After polishing the samples, large unconnected aluminum deposits were revealed, as shown in Fig. 1.8 (a), and these deposits could be easily removed with dilute hydrochloric acid. After removing all aluminum deposits, the thickness of the samples is about 100–200 microns, and no quantum oscillations were observed to 45 T.

This experiment demonstrates that quantum oscillations in flux-grown SmB_6 originates from flux inclusions; however, the original aluminum pellet used in the growth is polycrystalline. To solve this apparent contradiction, one needs to take into account the fact that aluminum also crystallizes in a cubic structure with a lattice parameter that is only 2% smaller than that of SmB_6 . In fact, x-ray tomography performed previously by a third group showed the presence of several aluminum deposits co-crystallizing with the SmB_6 host in typical millimeter-sized samples Fig. 1.8 (a) [7]. Precisely because several aluminum deposits may exist within one large SmB_6 single crystal, the amplitude of the quantum oscillation pattern may not be C_4 symmetric if the deposits are not perfectly aligned. In section 1.5.2, we will discuss bulk quantum oscillation results in floating-zone samples.

1.4.4 Angle-resolved photoelectron spectroscopy

A detailed overview of angle-resolved photoemission spectroscopy measurements on SmB_6 is beyond the scope of this book chapter. In principle, spin- and angle-resolved photoemission spectroscopy would be one of the most direct ways of probing the surface state

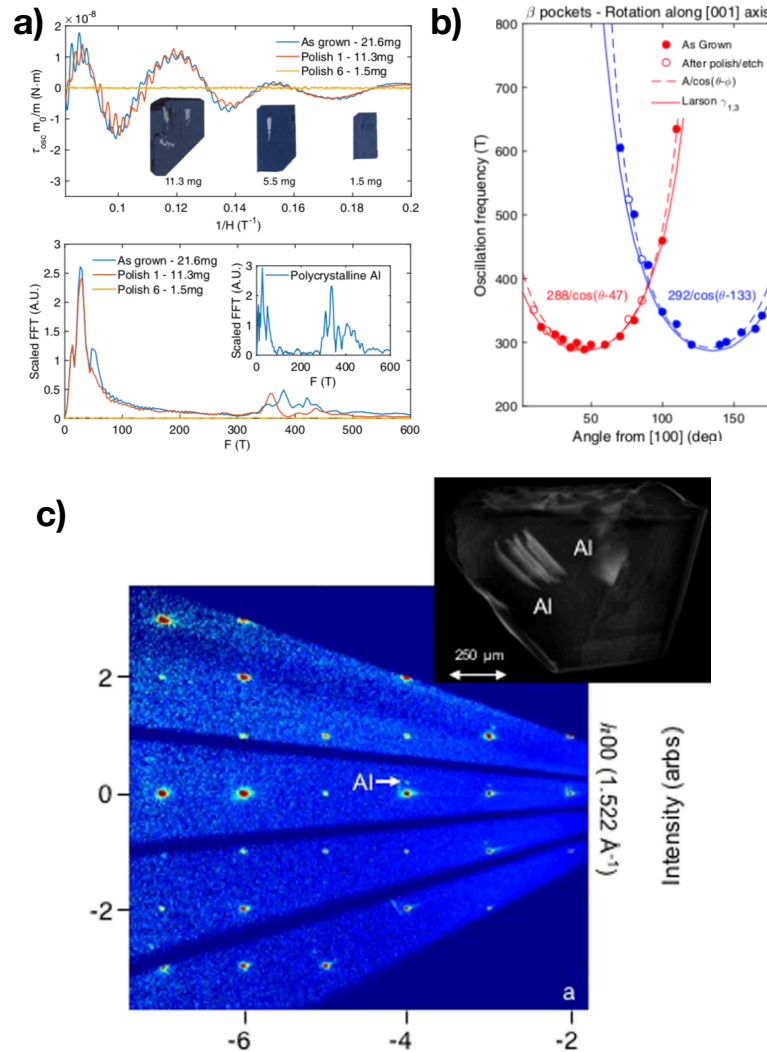
18 Chapter 1 Bulk and surface properties of SmB_6 

Figure 1.8 (a) Thickness dependence of the oscillatory torque in a flux-grown SmB_6 crystal. (b) FFT of the oscillatory torque. The FFT was scaled by the sample mass. Inset shows the FFT of polycrystalline Al. Reproduced from Thomas *et al.* [76]. (b) Angular dependence of the oscillation frequency compared with the $1/\cos\theta$ behavior as well as with the early report on Al by Larson and Gordon [77]. (c) Diffraction pattern of a flux-grown SmB_6 crystal and an x-ray computed tomography image showing the presence of aluminum inclusions. Reproduced from Phelan *et al.* [7].

dispersion and spin texture; however, the issues with surface terminations mentioned above as well as the small hybridization gap of SmB_6 hinder a consensus.

As in the case of scanning tunneling microscopy, there are reports in favor of either topologically protected surface states [78–81] or trivial surface conductivity [53,82]. For recent reviews of the subject, we invite the reader to refer to [62,65,83,84].

1.4.5 Thin films and nanowires

Though this chapter focuses on bulk and surface properties of SmB_6 single crystals, in this section we give a brief overview of recent efforts into the synthesis and characterization of SmB_6 thin films and nanowires. Early reports on thin film synthesis can be found in Refs. [85,86]. In 2014, polycrystalline SmB_6 thin films were synthesized by co-sputtering of SmB_6 and boron target within a combinatorial composition-spread approach [87]. A similar approach was used in 2017 by Petrushevsky *et al.* [88]. Growth attempts using pulsed laser deposition, molecular beam epitaxy or sputtering using a single target often result in thin films with substantial boron deficiency [87,89,90]. Batkova *et al.*, however, have recently reported the preparation of stoichiometric SmB_6 thin films via pulsed laser deposition [91].

Electrical resistance measurements on SmB_6 thin films typically display a semiconducting behavior with a resistance ratio, $R_{2\text{K}}/R_{300\text{K}}$ much smaller than that of the bulk, in agreement with the larger surface-to-bulk ratio [87,91]. Initial point-contact spectroscopy using a superconducting tip revealed the presence of Andreev reflection, suggesting the presence of surface states and of a transparent SmB_6 /superconductor interface [87]. Further evidence for a transparent interface was obtained by *in situ* deposition of superconducting Nb layers [92]. On one hand, magnetotransport as well as penetration depth measurements on SmB_6 thin films were argued to be consistent with topological surface states [93,94]. On the other hand, Li *et al.* observe that the electrical resistivity of SmB_6 thin films is thickness dependent, in apparent contradiction with the surface conductivity scenario [95]. Li *et al.* also show that SmB_6 thin films display large spin-orbit torque. Nevertheless, a

recent point-contact spectroscopy measurement reports the observation of perfect Andreev reflection in a heterostructure formed by insulating SmB_6 and superconducting YB_6 . This observation was understood as a manifestation of Klein tunneling due to the proximity-induced superconducting state in a topological insulator [96].

Rare-earth hexaboride nanowires have been synthesized by a variety of methods including vapor-liquid-solid mechanism [97, 98], chemical vapor deposition with [99] and without [100] a catalyst, and palladium-nanoparticle-assisted chemical vapor deposition [101]. Electrical resistance measurements are argued to be consistent with the presence of topological surface states [102–105].

1.5 Bulk properties

1.5.1 *ac electrical conductivity*

As discussed in section 1.4.1, the bulk of flux-grown SmB_6 has been shown to be remarkably insulating, with a 10-order-of-magnitude increase in dc resistivity on cooling from room temperature to 2 K. The bulk ac conductivity of SmB_6 , however, is several orders of magnitude larger than that of any known impurity band, and this is the next puzzle we would like to address.

Because of the large index of refraction of hexaborides and the particularly large ac conduction in SmB_6 , previous optical measurements were typically performed in reflection mode, relying on the Kramers-Kronig transformation [106–110]. Further, temperature- and thickness-dependent transmission experiments were missing until the renewed interest in SmB_6 . Early low-temperature ac conductivity measurements on floating-zone SmB_6 in the range from 0.6 to 4.5 meV provided evidence for a 19 meV energy gap and an additional narrow donor-type band at 3 meV below the conduction band [111]. The properties of SmB_6 below 8 K were first attributed to localized carriers in the narrow band responsible for hopping conductivity [111] and later to exciton-polaron complexes [112].

High-resolution optical measurements in the terahertz frequency range were recently performed to revisit these results. Lau-

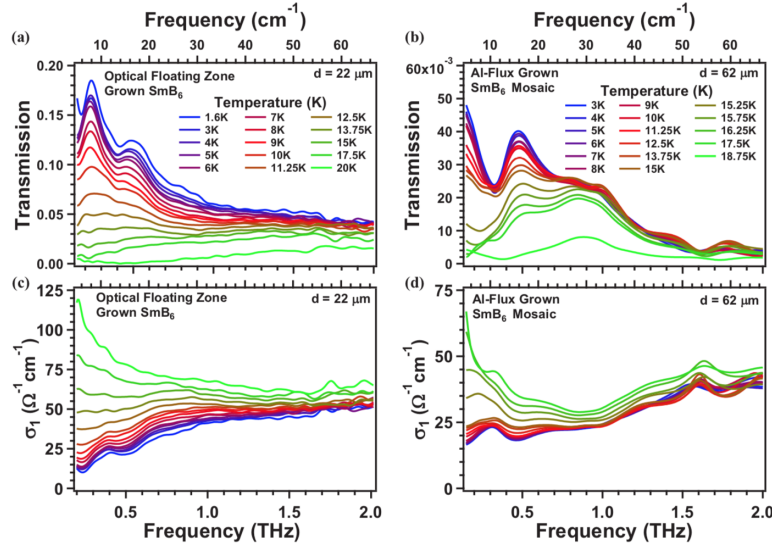


Figure 1.9 Frequency dependence of the complex transmission for (a) floating zone and (b) flux-grown SmB_6 single crystals with thickness of 22 and 62 μm , respectively. Frequency dependence of the real part of the optical conductivity for (c) floating zone and (d) flux-grown SmB_6 single crystals. Reproduced from Laurita *et al.* [113].

rita *et al.* investigated both floating zone and flux-grown samples with thicknesses smaller than 100 microns [113]. The experimental energy range, $\hbar\omega \approx 1-8$ meV, is smaller than the spectroscopic gap energy, which allows this technique to probe states within the bulk gap.

Figure 1.9 shows the frequency dependence of the complex transmission at various temperatures for floating-zone (panel a) and flux-grown (panel b) SmB_6 crystals, respectively. It is worth noting that flux-grown samples are smaller, and the required mosaic of samples displays worse signal to noise. Both real and imaginary parts of the complex optical conductivity are therefore extracted from the complex transmission, and the real part of the optical conductivity is shown in Fig. 1.9(c,d). At high temperatures, the optical conductivity displays a Drude-like response, i.e., σ_1 increases with decreasing frequency, indicating the presence of free charge carriers at E_F . Above 30 K, the sample becomes

22 | Chapter 1 Bulk and surface properties of SmB₆

opaque in the THz range. The magnitude of the Drude-like response decreases with decreasing temperature, in agreement with the opening of the hybridization gap. Below 13 K, the ac conductivity increases linearly with frequency before saturating at about 1 THz. This additional conduction channel is termed “localized” because it does not contribute to dc transport.

The pressing question here is whether this in-gap conduction is due to impurity states or to exotic neutral excitations, and answering this question is challenging. A recent analysis starts with the conjecture that the localized conductivity response is independent of temperature based on the weak temperature dependence of the conductivity at high frequencies [114]. The conductivity can be in turn modeled as a sum of the localized contribution, the Drude response, and a frequency-independent background. The latter term has been interpreted in previous measurements as a Mott minimum conductivity [111]. The dc conductivity can be extracted from the Drude response, providing an activated gap of 4.1 meV, in agreement with dc measurements discussed in section 1.4.1. The frequency independent conductivity is finite only above 12 K and reaches $9.4 \Omega^{-1}$ at 17.5 K.

The localized contribution within the gap dominates the conductivity response at 1.6 K. At about 1 THz (4 meV), the frequency dependence of the conductivity displays a crossover from $\sigma_1 \propto \omega^{0.8}$ to a linear dependence with frequency. The frequency dependence below the indirect gap is inconsistent with the weak Drude peak predicted by disordered Kondo insulator models, which take into account effects of substitution on the *f*-electron site above a percolation threshold [115, 116]. A sensible scenario, however, is that SmB₆ is below the percolation threshold, in which impurity states are localized. In addition, substitutional (point-defect) impurities might not be the only source of defects in SmB₆. A quantitative comparison between SmB₆ and localization driven insulators (e.g. Si:P at 40% doping) reveals that the in-gap ac conductivity of SmB₆ is about four orders of magnitude larger than the typical impurity band conduction, being comparable to completely amorphous alloys [117, 118]. This possibility brings up again the lack of a deep understanding of disorder in this material. In fact, a recent theoretical effort revisits the donor impurity band mechanism in SmB₆ tak-

ing into account its peculiar "mexican-hat-like" band structure and shows that the resulting impurity band is in many ways distinct from the conventional semiconductor case [37]. In particular, the critical doping concentration necessary to drive an insulator-metal transition is much larger than in the conventional case. Estimates of the ac conductivity in this framework are in agreement with the experimental results discussed above and provide an explanation for why SmB_6 is a robust dc insulator, but an ac conductor. The second sensible scenario is the presence of charge-neutral quasiparticles within the Kondo gap, which could couple to an ac electric field [31]. Though this scenario has been proposed theoretically, a qualitative prediction that matches the experimental power law behavior with frequency is missing. This scenario has been also suggested by quantum oscillation and thermal conductivity measurements on floating zone samples, as we will discuss in the next two sections. Finally, we note that the spectral weight of the in-gap conductivity provides further information on the density of charge carriers and effective mass *via* the conductivity sum rule relation. A rough estimate using the bare mass of the electron gives a charge density of about 1 electron per 1000 unit cells, which is roughly consistent with both an impurity contribution as well as a neutral Fermi surface. Other experimental probes are therefore required to answer this question.

1.5.2 Quantum oscillations

Shortly after the report of quantum oscillations in flux-grown SmB_6 , which we discussed in section 1.4.3, similar torque magnetometry experiments were performed on floating-zone crystals [119]. The first key remark is that the oscillatory behavior shown in Fig. 1.10 (a) is *not* observed in every floating-zone sample. This is an outstanding question which calls for immediate attention, especially considering that flux-grown samples free of aluminum do not show quantum oscillations and that floating-zone rods host compositional changes that are not fully understood.

When quantum oscillations are present in floating-zone samples, they are observed at high frequencies and are independent of the surface details. Further, the angular dependence of the oscilla-

24 | Chapter 1 Bulk and surface properties of SmB_6

tions resembles those of LaB_6 and PrB_6 , as shown in Fig. 1.10 (c). Taken together, these observations are inconsistent with surface-driven quantum oscillations and suggest a bulk origin.

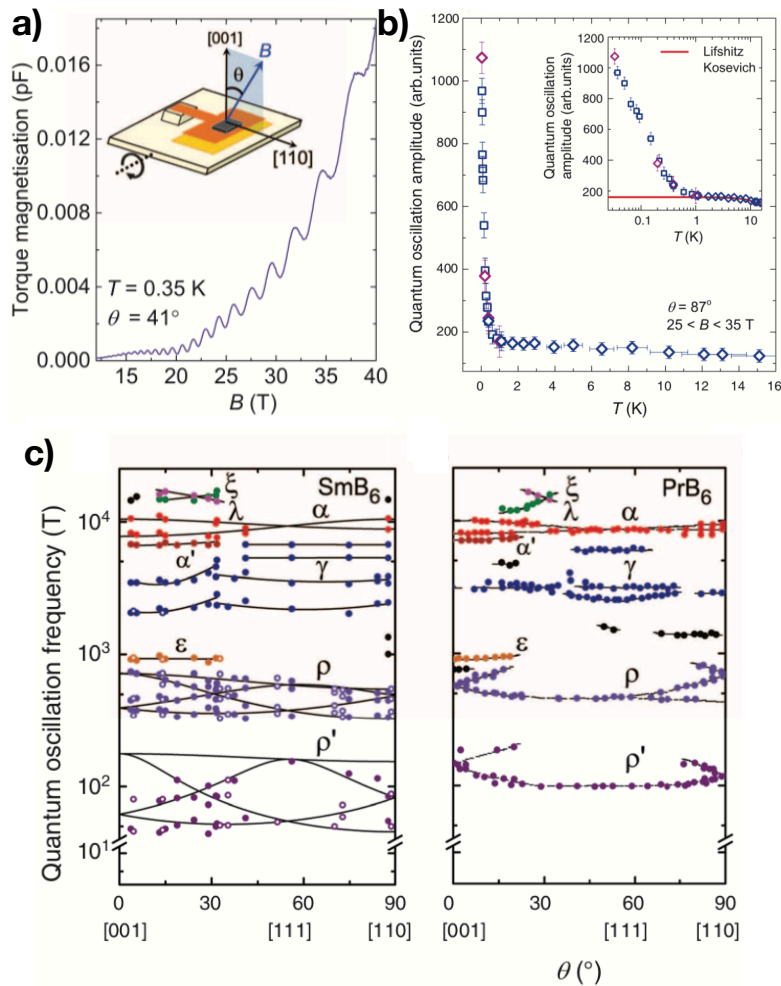


Figure 1.10 (a) Torque signal of a floating-zone SmB_6 crystal as a function of magnetic field. (b) Quantum oscillation amplitude as a function of temperature. (c) Angular dependence of the quantum oscillation frequency for SmB_6 and PrB_6 . Reproduced from Tan *et al.* [119].

Quantum oscillations in floating-zone samples were termed “unconventional” owing to the temperature dependence of the quantum oscillation amplitude, shown in Fig. 1.10 (b). Above 1 K, the amplitude follows the conventional Lifshitz-Kosevich formula [120] with a small effective mass (0.1-0.8 m_e); however, below 1 K the amplitude increases greatly down to base temperature. Importantly, oscillations in the dc electrical resistivity are not observed.

As in the case of ac conductivity measurements, we are again faced with (at least) two possibilities. The first one is that quantum oscillations may arise from spatially unconnected metallic patches from a secondary unknown phase, similar to the aluminum inclusions observed in flux-grown samples. Though Tan *et al.* state that this possibility appears to be unlikely, it cannot be ruled out at this point. The second possibility is the presence of low-energy neutral excitations within the charge gap of SmB₆. Hartstein *et al.* find that the density of states obtained from their quantum oscillation Fermi surface matches that of specific heat measurements ($\gamma \sim 4(1) \text{ mJ/mol.K}^2$) [121]. The steep increase in the low-temperature quantum oscillation amplitude also resembles the increase in the specific heat. Further, the low-temperature entropy obtained from the oscillatory pattern remains finite below 1 K, indicating a finite density of states. These observations, combined with thermal conductivity measurements to be discussed in the next section, were taken as evidence for bulk itinerant low-energy excitations that couple to magnetic fields, but not weak dc electric fields.

1.5.3 Thermal conductivity

Thermal conductivity (κ) measurements are a valuable way of probing possible fermionic charge-neutral excitations, which carry entropy and would contribute to a finite residual term, κ_0/T , in the $T = 0$ limit. Previous experiments performed almost 40 years ago concluded that the thermal conductivity of SmB₆ above 1.5 K is dominated by phonons, i.e., $\kappa/T \propto T^2$ [123], but this scenario has been revisited recently in experiments performed at much lower temperatures and much higher magnetic fields.

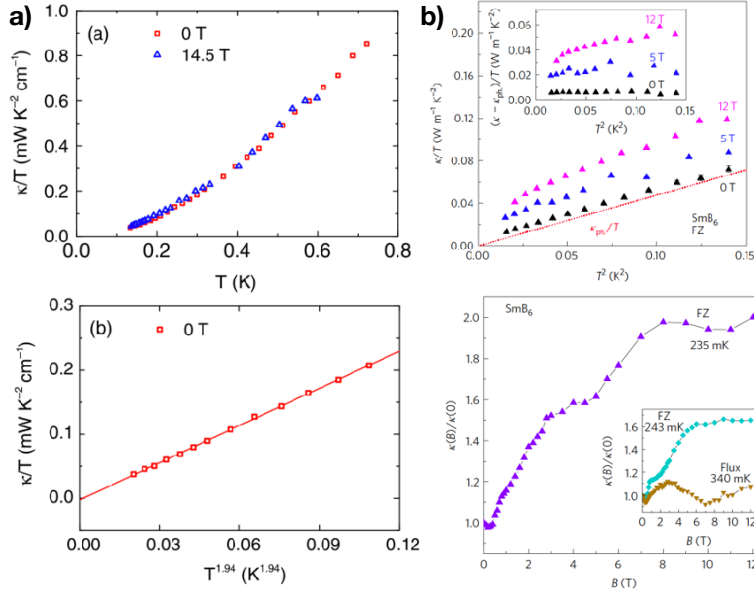
26 | Chapter 1 Bulk and surface properties of SmB₆

Figure 1.11 (a) Thermal conductivity of a flux-grown SmB₆ sample vs. temperature (top) and $T^{1.94}$ (bottom). Reproduced from Xu *et al.* [122]. (b) Thermal conductivity of a floating-zone SmB₆ sample vs. T^2 (top) and magnetic field (bottom). Reproduced from Hartstein *et al.* [121].

The first contemporary report was performed on flux-grown SmB₆ single crystals in a dilution refrigerator with fields to 14.5 T [122]. The thermal conductivity was measured on a (100) surface using a standard four-wire steady-state method with two RuO₂ chip thermometers. Figure 1.11a displays thermal conductivity data down to 0.1 K in zero field and at 14.5 T. By fitting the zero-field data to $\kappa/T = a + bT^{\alpha-1}$, one extracts a residual term $\kappa_0/T = -0.003 \pm 0.004 \text{ mW K}^{-2}\text{cm}^{-1}$, which is zero within the experimental error bar. The contribution from surface states is estimated to be two orders of magnitude smaller than this error bar and therefore negligible.

As shown in Fig. 1.11 (a) (bottom panel), $\alpha = 2.94$, in agreement with the expected phonon contribution. Finally, applied magnetic fields have very little effect on the thermal conductivity, and the residual term κ_0/T remains negligible. Xu *et al.* therefore conclude

that thermal conductivity measurements do not support fermionic charge-neutral quasiparticles. One possible scenario raised by Xu *et al.* to explain the bulk quantum oscillation results discussed above is spatial inhomogeneity below a percolation threshold.

An independent report on floating-zone crystals, however, reveals a finite zero-field κ_0/T , which increases as a function of applied field as shown in Fig. 1.11 (b) [121]. Hartstein *et al.* argue that phonons are unlikely to be the origin of this behavior because the phonon thermal conductivity is at its maximum in the boundary scattering limit. The similarity between the field dependent thermal conductivity of SmB_6 and that of organic insulator $\kappa\text{-(BEDT-TTF)}_2\text{Cu}_2(\text{CN})_3$ is argued to be evidence for a neutral Fermi surface hosting excitations that transport heat but not charge.

A recent report by a third group sheds light on this controversy by measuring field-dependent thermal conductivity down to 70 mK on a variety of single crystals grown by both flux-grown and floating-zone techniques [124]. The authors confirm the absence of a residual term κ_0/T on six different samples in both zero field and at high magnetic fields, as summarized in Fig. 1.12. A large field-induced enhancement of κ , however, is observed for all floating zone samples as well as two out of three flux-grown samples. Importantly, this sample dependence points to an extrinsic origin.

In addition, the field-induced enhancement of κ is systematically smaller in flux-grown samples, and the behavior of sample F3 is in agreement with the first report discussed above [122]. Generally speaking, the field dependence of the thermal conductivity is consistent with two distinct mechanisms: low-energy magnetic excitations (e.g. magnons or spinons) or phonons scattered by a field-dependent contribution (e.g. spin fluctuations or magnetic impurities). The authors conclude that their data is in line with the latter scenario as magnetic impurities may significantly affect the phonon thermal conductivity in insulators even at a 1% level. The application of magnetic field splits the energy levels of the magnetic impurities, which causes a mismatch between the phonon energy and the impurity level splitting. To test their interpretation, the authors reduced the cross-sectional area of one of the floating zone samples, which makes the boundary-limited phonon conduc-

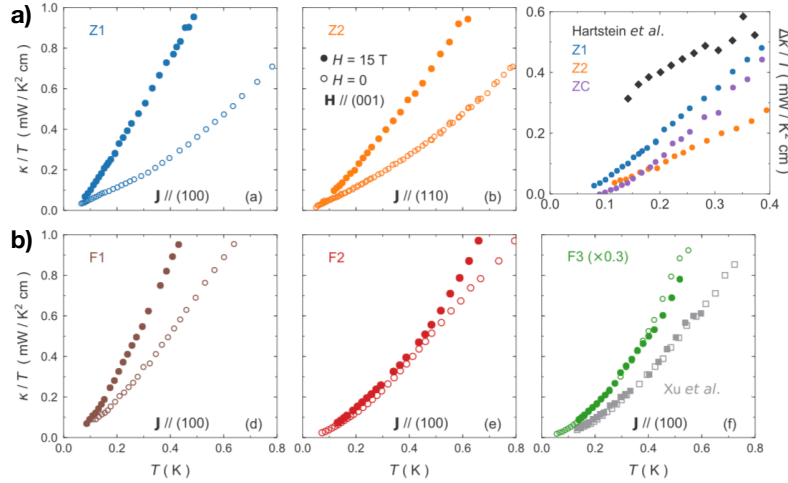
28 | Chapter 1 Bulk and surface properties of SmB_6 

Figure 1.12 Temperature dependence of the thermal conductivity for (a) floating-zone and (b) flux-grown SmB_6 crystals. Reproduced from Boulanger *et al.* [124]. The references to Hartstein *et al.* in (a) and Xu *et al.* in (b) correspond to Refs. [121] and [122], respectively.

tivity smaller. According to their expectation, κ/T^2 decreases with decreasing cross section because the magnetic field gaps out the zero-field scattering mechanism, and the thermal conductivity is then set by the boundary limit. For more details on the analysis, including the high-temperature regime, please refer to [124]. It is also worth noting that, though there is no evidence for fermionic neutral quasiparticles, they may be thermally decoupled from the measurable, heat-carrying phonons.

1.5.4 Specific heat

Figure 1.13 (a) shows a compilation of specific heat data on a variety of samples grown using different methods [76,119,121,125–127]. Similar to the ac and thermal conductivity measurements discussed above, specific heat measurements are sensitive to impurities that may not percolate in dc resistivity measurements. In fact, the large variation of the residual specific heat in Fig. 1.13 (a) points to an extrinsic origin. The lowest specific heat magnitude reported to date was obtained on a crystal grown with isotopically

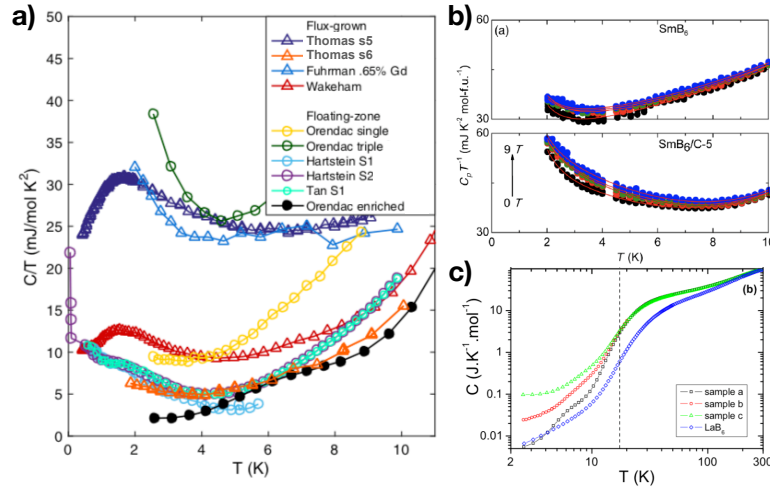


Figure 1.13 (a) A compilation of zero-field specific heat data as a function of temperature for SmB_6 crystals grown by different techniques [76, 119, 121, 125–127]. Reproduced from Thomas *et al.* [76]. (b) Zero-field specific heat data of carbon-doped floating-zone SmB_6 . Reproduced from Phelan *et al.* [52]. (c) Zero-field specific heat data of floating-zone LaB_6 and SmB_6 . Sample a was grown with isotopically enriched elements, sample b with natural impurities and sample c with natural impurities and triply melted. Reproduced from Orendac *et al.* [127].

enriched ^{154}Sm and ^{11}B [127] providing further evidence that the broad feature centered near 1.5 K is caused by naturally occurring impurities. A residual feature, however, remains at about 7 K, and we will come back to this energy scale in section 1.5.7.

Rare-earth purification is challenging and expensive. Rare-earth elements obtained from Ames Laboratory are one of the purest available sources, but Ames samarium is still 99.99% pure at best. Typically, europium, erbium, lanthanum and iron can be found at several ppm level. In agreement with this reasoning, enhanced low-temperature specific heat values are observed in flux-grown samples intentionally doped with gadolinium. In addition, specific heat data from samples with distinct Gd concentrations can be scaled to follow the same power law at low temperatures [125]. This scaling was argued to be consistent with the Kondo impurity model. We note that enhanced values of the low-temperature

30 | Chapter 1 Bulk and surface properties of SmB_6

specific heat are also observed in floating-zone samples doped with carbon [52]. Further, floating-zone samples that are doubly or triply melted display similar specific heat enhancement, though in this case it is less clear what exact type of defects one would encounter [127].

Attempts to fit the specific heat above 2 K have been made by independent groups typically including a combination of the standard electronic (γT) and lattice (βT^3) contributions as well as an exchange-enhanced paramagnetic term ($\alpha T^3 \ln(T/T^*)$) and the Schottky anomaly (AT^{-2}) [52, 127]. Phelan *et al.* showed that the phonon and exchange terms follow a universal curve with a characteristic temperature $T^* = 17$ K associated with Kondo hybridization. Below 2 K, however, additional contributions come into play. Previous specific heat measurements performed in dilution refrigeration temperatures successfully explained the *difference* between in-field and zero-field measurements by calculating the contributions from nuclear magnetic moments of ^{147}Sm , ^{149}Sm , ^{10}B and ^{11}B isotopes as well as 300 ppm of magnetic impurities [128]. A quantitative understanding of the anomalous bulk behavior of SmB_6 even at zero field, however, remains unavailable [126, 129].

1.5.5 Raman spectroscopy

Now we turn our attention to spectroscopic techniques. Raman spectroscopy is based on the inelastic scattering of light in a material, providing a direct means of probing the development of an energy gap. This technique also provides energy and symmetry information about other low-frequency excitations including crystal-field excitations, excitons, and anomalous phonons. Evidence for an energy gap in SmB_6 was observed in early reports of the temperature dependence of the Raman continuum scattering, as shown in Fig. 1.14 (a) [130]. The electronic scattering intensity shifts abruptly below $T^* \approx 50\text{--}60$ K, which corresponds to the temperature at which the magnetic susceptibility peaks. The shift in spectral weight is centered about an isosbestic point at 290 cm^{-1} , an energy substantially larger than the energy scale over which the gap appears in the scattering response. A number of theoretical models were proposed to account for electrical transport as well as

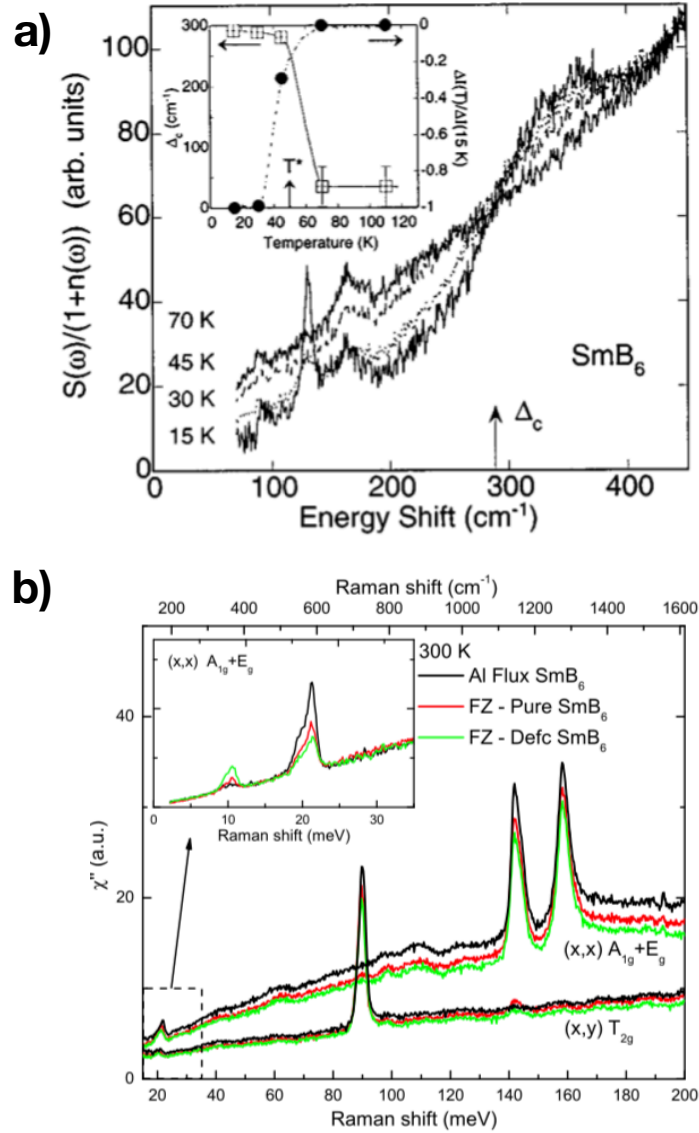


Figure 1.14 Raman scattering response function of a flux-grown SmB_6 single crystal at various temperatures (panel a). Reproduced from Nyhus *et al.* [130]. Raman scattering response function of both flux-grown and floating-zone crystals at room temperature (panel b). Reproduced from Valentine *et al.* [131].

32 | Chapter 1 Bulk and surface properties of SmB₆

Raman data [132]; however, the discovery of non-Ohmic behavior arising from a conducting surface state in SmB₆ discussed above makes analysis not taking this into account of limited value.

In the past few years, the Raman response of SmB₆ was revisited, and a timely sample dependence investigation was performed [131]. Figure 1.14 (b) shows the room temperature Raman spectra of three distinct single crystals: one crystal grown by the flux technique (Al flux SmB₆), a second crystal grown by the floating zone technique close to being stoichiometric (FZ SmB₆ - Pure), and a third crystals also grown by the floating zone technique but less stoichiometric (FZ SmB₆ - Defc). As we mentioned above, an increase in the number of Sm vacancies is observed along the length of a floating zone crystal rod due to the vaporization and has been characterized by a systematic decrease in lattice parameters.

Three symmetry-allowed phonons are observed in Fig. 1.14 (b), in agreement with previous reports [133]. These narrow peaks are related to distortions of the B₆ octahedra as follows: T_{2g} phonon at 89.6 meV (723 cm⁻¹), E_g phonon at 141.7 meV (1143 cm⁻¹), and A_{1g} phonon at 158.2 meV (1277 cm⁻¹). At much lower energies, however, two additional features appear at 10 meV and 21 meV, which are not allowed by the cubic space group in first-order Raman scattering. The latter feature has been previously assigned to a two-phonon scattering mode [130]. The former feature, however, has been recently attributed to a finite-momentum scattering from acoustic phonons due to local symmetry breaking induced by the presence of Sm defects [131]. Neutron scattering experiments show a relatively flat dispersion of the acoustic phonon branches, in agreement with the narrow line width at 10 meV [134]. Further evidence for this scenario comes from the 50% increase in spectral weight at 10 meV in the most deficient floating-zone sample, which is estimated to have only about 1% of Sm vacancies. A significant impurity-driven enhancement is also observed in the specific heat of these samples [135].

1.5.6 X-ray, neutron and Mössbauer spectroscopies

Early L_3 -edge x-ray absorption experiments [138] as well as ¹⁴⁹Sm Mössbauer resonance measurements [137, 139] estimated the va-

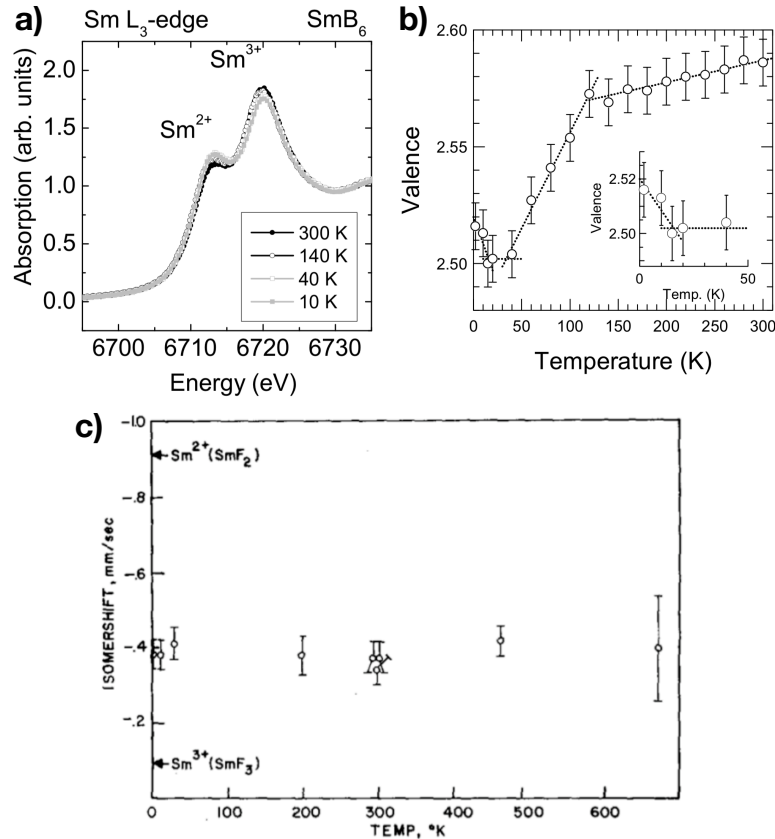


Figure 1.15 (a) Sm L_3 -edge x-ray absorption spectra at different temperature. Reproduced from Mizumaki *et al.* [136]. (b) Average Sm valence as a function of temperature. Reproduced from Mizumaki *et al.* [136]. (c) Isomer shift as a function of temperature. Reproduced from Cohen *et al.* [137].

lence of Sm to be +2.6 at room temperature. X-ray absorption spectra display two separate peaks corresponding to Sm^{2+} and Sm^{3+} [136]. The spectra evolve with temperature as shown in Fig. 1.15 (a, b), revealing that the valence of Sm decreases with decreasing temperature. The temperature dependence of the lattice parameters [140] combined with negative thermal expansion and anomalous elastic constants at low temperatures [141, 142] also

indicate valence changes as a function of temperature. Mössbauer resonance, however, only contains a single-line spectrum, and no change in the Sm valence as a function of temperature is detected by isomer shift measurements, Fig. 1.15 (c). This apparent contradiction can be resolved by taking into account the different time scales of these two measurements. X-ray absorption is a faster measurement (10^{-12} s) than Mössbauer resonance (10^{-8} s), indicating that the valence of Sm fluctuates at about 10^{-8} s. An alternative explanation, however, has been recently proposed based on the boron-dimer model discussed in section 1.3 [20]. The authors predict a constant ratio of *f*-shell occupations, which is in turn probed by Mössbauer spectroscopy, and a variable *d*-orbital occupation, which cannot be probed by Mössbauer measurements. We note that the Sm valence obtained from the above Sm *L*₃ x-ray absorption spectroscopy results has been reproduced by several independent groups as well as by distinct methods including x-ray photoelectron spectroscopy [143–146]. The Mössbauer isomer shift result has been also recently revisited and reproduced by Tsutsui *et al.* [147].

Resonant x-ray emission spectroscopy as well as x-ray absorption spectroscopy also have been employed to investigate the valence of SmB₆ under applied pressure. Electrical resistivity measurements under hydrostatic conditions show that the insulating gap of SmB₆ vanishes at $P_c = 10$ GPa accompanied by magnetic order [148]. This critical pressure is dependent on the hydrostaticity of the pressure media and may be as low as ~ 4 GPa in quasi-hydrostatic environments [149–151]. X-ray spectroscopy measurements report the increase in Sm valence under pressure towards the trivalent state as the system goes towards the antiferromagnetic metallic ground state [152–156]. A discrepancy, however, is observed in the quantitative analysis by different groups. For example, Zhou *et al.* report a valence very close to 3+ at 20 GPa [154], whereas other groups argue for a finite divalent character to 35 GPa [153, 155, 157].

Sm *M*-edge x-ray absorption and x-ray magnetic circular dichroism measurements have been simultaneously performed on the surface and in the bulk of SmB₆, respectively. Phelan *et al.* confirm the presence of Sm²⁺ and Sm³⁺ in the bulk of floating-zone

crystals; however, the polished surface is shown to contain mostly Sm^{3+} with a net magnetic moment of $0.09 \mu_B$ at $T = 10$ K. The authors argue that the discrepancy between the valence at the surface and in the bulk could generate band bending at the interface. Though Chen *et al.* also report a higher Sm valence at the surface of powdered floating-zone SmB_6 , the extracted value of $\nu = 2.7$ is below the trivalent state [155]. Employing the same techniques on vacuum-cleaved samples reveal that both divalent and trivalent Sm are present on the surface of SmB_6 , indicating that polishing has a significant effect on the surface valence [158]. In addition, Fuhrman *et al.* report that the Sm^{3+} magnetic dipole moment antialigns with an applied magnetic field below $T = 75$ K and suggest that Sm^{3+} couples antiferromagnetically to large-moment paramagnetic impurities known to be present in the samples. Sm N -edge x-ray absorption spectroscopy has also been performed on flux-grown SmB_6 [159]. He *et al.* show that the Sm^{3+} contribution on a cleaved surface increases irreversibly with time as it ages in an ultra-high-vacuum chamber. In fact, soft x-ray absorption and reflectometry measurements on floating-zone crystals reveal that a cleaved (001) surface of SmB_6 undergoes significant valence and chemical reconstruction as a function of time. The final surface is argued to be boron-terminated with a Sm^{3+} subsurface region. At room temperature, this reconstruction takes less than two hours, whereas below 50 K it takes about a day [68]. These results shed light on discrepancies observed in scanning tunneling spectroscopy measurements discussed in section 1.4.2.

Recent non-resonant and resonant x-ray scattering experiments provide a powerful tool to determine the ground state and crystal field splitting of SmB_6 , respectively. On one hand, core-level non-resonant scattering in the hard x-ray region is a bulk sensitive spectroscopic technique performed at large momentum transfer. The scattering function therefore provides information on higher multipole terms and allows the determination of the ground state wave function even in cubic compounds [160]. On the other hand, $M_{4,5}$ -edge ($3d \rightarrow 4f$) resonant inelastic x-ray scattering is both element- and configuration-sensitive and allows the determination of the crystal field splitting of the Sm^{3+} Hund's rule ground state [161]. These two spectroscopic techniques find that the $J = 5/2$

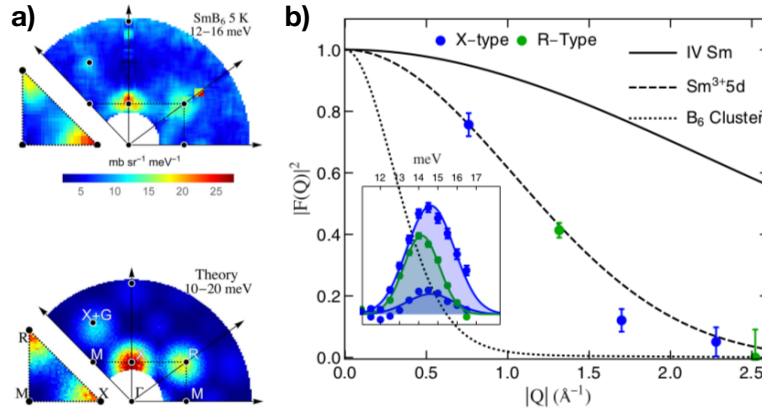


Figure 1.16 (a) Experimental (top) and theoretical (bottom) energy-integrated neutron scattering intensity of floating-zone $^{154}\text{Sm}^{11}\text{B}$ at high-symmetry planes. (b) Comparison between the squared magnetic form factor of different scattering centers (lines) and the experimental integrated neutron scattering intensity (symbols) as a function of momentum \mathbf{Q} . Reproduced from Fuhrman *et al.* [166].

multiplet of $\text{Sm } f^5$ splits into a Γ_8 quartet ground state and a Γ_7 first excited doublet at 20 meV. It is worth noting that this crystal field splitting agrees well with the expected splitting from the extrapolation of crystal field parameters obtained within the RB_6 series (R is a rare-earth element).

Inelastic neutron scattering has been also employed to shed light on this problem. The strong neutron absorption of both samarium and boron, combined with the presence of hybridization and two Sm configurations, makes these measurements challenging. Nevertheless, early inelastic neutron scattering experiments using double isotopic samples, $^{154}\text{Sm}^{11}\text{B}$, identify broad intermultiplet transitions at about 36 meV and 130 meV as well as a narrow low-energy excitation at the R point $[(\frac{1}{2} \frac{1}{2} \frac{1}{2})]$ centered at 14 meV only observed at temperatures below 100 K [134, 162–165]. This low-temperature feature does not follow the localized f -electron form factor and was therefore argued to be caused by the mixed-valence state of Sm and exciton states within the gap.

Recent inelastic neutron scattering measurements have revisited the low-energy, low-temperature features of SmB_6 in the entire

Brillouin zone [166]. Fuhrman *et al.* show that the narrow (> 2 meV) resonant mode at 14 meV is also intense near the X point ($\frac{1}{2}00$), see Fig. 1.16 (a), and, though much weaker, goes beyond the first zone. As a result, the form factor is mapped out and shown to unexpectedly follow the $5d$ electron form factor, Fig. 1.16 (b), indicating a critical role of such orbitals in the exciton formation and providing strong constraints to realistic theories. Fuhrman *et al.* propose a minimal phenomenological model with third neighbor hopping, which allows for $5d$ -electron “pseudo-nesting” to enhance the generalized susceptibility that appears in the inelastic neutron scattering measurements through interband transitions. This phenomenological model generates a band structure with inversion pockets at X, in agreement with the topological Kondo insulator picture.

The spin-exciton may also shed light on the presence of impurities in SmB_6 as coupling of the exciton to a fermionic density of states at E_F would cause a finite relaxation rate in inelastic neutron scattering measurements. A nearly temperature independent lifetime, however, is observed from 15 to 3.5 K, indicating no coupling to additional energy scales below the 14 meV spin-exciton mode. In addition, no indication of magnetism was observed in the low-energy spectrum, and an upper bound fluctuating moment of $0.05(2) \mu_B^2$ was estimated. The authors conclude that magnetic impurities in SmB_6 may be screened.

1.5.7 Nuclear, electron and muon spin resonance

Nuclear magnetic resonance takes advantage of the nonzero nuclear spin moment of many stable isotopes to obtain local information on the internal field as well as spin dynamics in a material. Though it is challenging to detect Sm nuclei in SmB_6 , resonance lines from ^{11}B are easy to detect and allow an indirect measure of the Sm mixed valence through the hyperfine interaction. Early nuclear magnetic resonance measurements by Peña *et al.* showed that the ^{11}B spin lattice relaxation above 15 K is activated with an energy gap of about 6 meV, in rough agreement with the transport gap (i.e., 4 meV) [167, 170]. An anomalous peak, however, emerges at about 5 K as shown in Fig. 1.17 (a). The authors state that evalu-

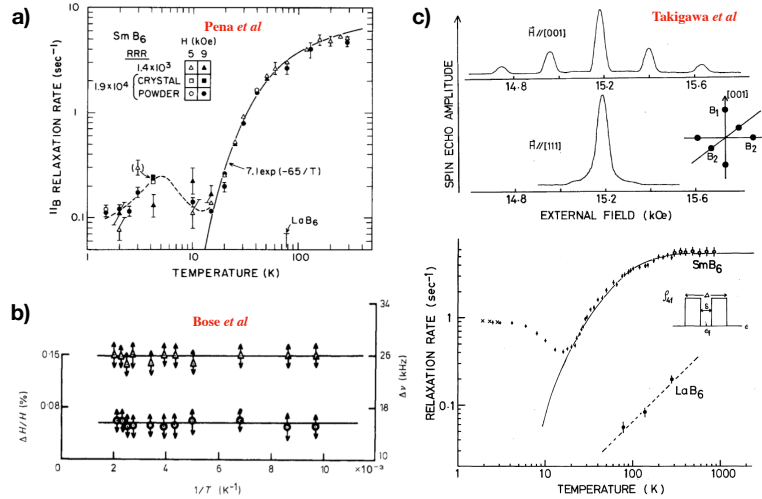
38 | Chapter 1 Bulk and surface properties of SmB_6 

Figure 1.17 (a) ^{11}B relaxation rate as a function of temperature in flux-grown powdered SmB_6 . Reproduced from Peña *et al.* [167]. (b) NMR linewidth as a function of inverse temperature. Reproduced from Bose *et al.* [168]. (c) Spin-echo spectra at 4.2 K and 20.7 MHz (top) and ^{11}B relaxation rate (bottom) of a SmB_6 single crystal. Reproduced from Takigawa *et al.* [169].

ation of models for this anomaly is hindered by the lack of precise defect characterization in nearly pure SmB_6 , and this statement remains accurate to date. Peña *et al.* argue that the maximum may be related to a decrease in fluctuation amplitude at low temperatures, which in turn could be caused by Sm^{3+} formation near Sm vacancies.

A second ^{11}B nuclear magnetic resonance experiment reported constant Knight shift and line width data from 100 K to 480 K [168]. Bose *et al.* ascribed this result to a temperature independent valence fluctuation of the Sm ion owing to the fast fluctuation rate ($< 10^{13} \text{ s}^{-1}$), Fig. 1.17 (b). A third set of ^{11}B nuclear magnetic resonance measurements were carried out by Takigawa *et al.* at low fields and at temperatures between 2.5 K and 850 K, as shown in Fig. 1.17 (c) [169]. The temperature dependence of the relaxation rate above 20 K was modeled taking into account a 50 K gap, and they attribute the increase in $1/T_1$ below 15 K to the Wigner crystal

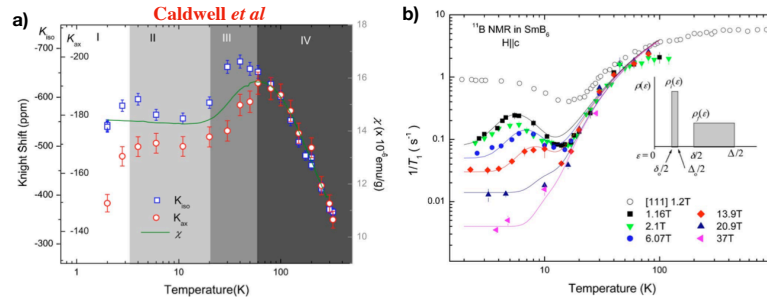


Figure 1.18 (a) NMR Knight shift as a function of temperature. (b) ^{11}B relaxation rate as a function of temperature in flux-grown SmB_6 single crystals for various applied fields along the c -axis. Reproduced from Caldwell *et al.* [171].

scenario. These data are similar to those reported by Peña *et al.*; however, $1/T_1$ plateaus below 5 K, instead of decreasing with decreasing temperature, which could be due to an anisotropy in the relaxation rate. It is worth noting that Peña *et al.* powdered a collection of flux-grown single crystals for the experiments, whereas the sample preparation procedure was not described by Bose *et al.* and Takigawa *et al.*

In 2007, nuclear magnetic resonance measurements in flux-grown SmB_6 single crystals were reported in high magnetic fields to 37 T [171]. Caldwell *et al.* confirm the opening of a gap in the density of states below 100 K and the presence of in-gap states, which dominate the nuclear relaxation below about 10 K, as shown in Fig. 1.18. The application of high magnetic fields suppress this in-gap contribution, whereas the gap remains open to 37 T. The authors model their data with a gapped density of states containing a symmetric rectangular distribution of in-gap states as shown in Fig. 1.18 (b). This simplified density of states is able to fit the experimental data, though the nature of the field-dependent in-gap states remains unclear. The authors argue that an impurity band caused by boron vacancies is not consistent with the significant field dependence of the data. We note that it could be useful to revisit these measurements in light of the recent information on surface states, spin excitons and magnetic impurities. For a recent theoretical perspective on this issue, please refer to [172].

40 | Chapter 1 Bulk and surface properties of SmB_6

Nuclear magnetic resonance measurements on floating-zone SmB_6 have been performed under hydrostatic pressures to 5 GPa [173–175]. The temperature dependence of the spin lattice relaxation remains activated under pressure, though the insulating gap is reduced by about 30% at 5 GPa. As discussed in the previous section, the gap collapse is consistent with dc electrical resistivity measurements and is related to an increase of the Sm valence towards a trivalent state [152–154, 156].

As with nuclear magnetic resonance, muon spin resonance is also a sensitive local magnetic probe, which could shed light on the nature of the in-gap states in SmB_6 . Polarized muon particles—subatomic particles similar to the electron but two hundred times heavier—are implanted in the bulk of the samples, and the asymmetry of the muon decay in time is measured. To our knowledge, the first muon spin resonance measurements in SmB_6 were re-

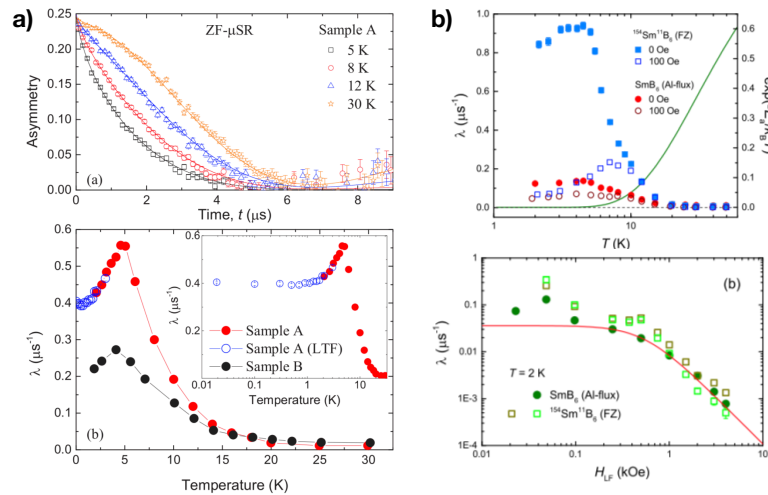


Figure 1.19 (a) Top: Zero-field muon spin resonance asymmetry signal of floating-zone SmB_6 . Bottom: Temperature dependence of the muon spin relaxation rate of floating-zone SmB_6 (sample A) and flux-grown SmB_6 (sample B). Reproduced from Biswas *et al.* [176]. (b) Top: Muon spin relaxation rate at zero field (solid symbols) and 100 Oe (open symbols) of floating-zone SmB_6 (FZ) and flux-grown SmB_6 (Al flux). Bottom: Field dependence of the relaxation rate obtained from fits of the asymmetry spectra at 2 K. Reproduced from Gheidi *et al.* [177].

ported in 2014 [176]. Biswas *et al.* observe homogeneous magnetic field fluctuations in the bulk of SmB_6 below about 15 K in both floating-zone and flux-grown samples, as shown in Fig. 1.19 (a). The similarity between this temperature scale and those of nuclear magnetic resonance discussed above indicate a common origin. We note that no magnetic order was observed down to 19 mK. In a follow-up report, Biswas *et al.* attribute the observed magnetic excitations to spin excitons in the bulk of SmB_6 . These spin excitons produce local magnetic fields of about 1.8 mT fluctuating on a time scale of about 60 ns. The authors find a suppression of these fluctuations at the surface and, as a result, a small enhancement in static magnetic fields [178]. According to the authors, the difference in magnitude of the asymmetry decay between floating-zone and flux-grown samples could be coming from a nonrelaxing background signal in the small flux-grown samples or slightly different microscopic properties.

A recent report by an independent group, however, argues for the presence of sample-dependent quasi-static magnetism of extrinsic origin below about 10 K [177]. Gheidi *et al.*, however, also suggest the presence of intrinsic magnetism originated from two different sources, the first being an underlying low-energy weak fluctuating moment ($10^{-2} \mu_B$), and the second being consistent with a 2.6 meV bulk magnetic excitation gap at zero field [179, 180]. The question of why this magnetic excitation is not detected by inelastic neutron scattering remains open.

Electron spin resonance is also a local probe of paramagnetic ions in a materials. Though conduction-electron spin resonance has been reported in alkaline-earth hexaborides [181], this conduction-electron signal appears to be absent in SmB_6 . Intentional doping with paramagnetic probes is therefore required for the observation of a signal. Early electron spin resonance measurements of Er^{3+} in SmB_6 at 4.2 K were not consistent with a purely cubic symmetry [182]. This inconsistency was ascribed to dynamical Jahn-Teller effect on the cubic Γ_8 crystal-field ground state [183]. Recent experiments revisited this scenario and proposed that the small Er^{3+} ions experience anharmonic rattling vibrations instead [184]. Lesseux *et al.* also performed electron spin resonance measurements on SmB_6

42 | Chapter 1 Bulk and surface properties of SmB₆

crystals doped with Dy³⁺ and Nd³⁺, but no appreciable signal was observed.

Gd³⁺ is a powerful paramagnetic probe in electron spin resonance measurements owing to its $L = 0$ ground state. Early electron spin resonance measurements of Gd³⁺ in SmB₆ revealed an unusual electron spin resonance spectrum below 5 K, which could not be explained by the $4f^7$ configuration [185]. Wiese *et al.* argue for a divalent $4f^7 5d^1$ configuration for Gd owing to a trapped conduction electron. These experiments have been also revisited recently by Souza *et al.*, and the origin of the unusual Gd²⁺-like signal is found to be an oxide impurity phase on the surface of the crystal [186]. In the very dilute limit, the low-temperature fine structure of the Gd³⁺ electron spin resonance spectra follows the expected cubic crystal-field environment. At high temperatures, a single resonance is observed and follows an activation behavior with a gap of about 50 K. Though these experiments have thus far probed the bulk of SmB₆, electron spin resonance may also be sensitive to the surface of SmB₆, which invites further experimental work.

1.6 Concluding remarks

The current fundamental question regarding SmB₆ is whether it is actually a strongly correlated topological insulator, a question which still remains to be definitively resolved. It is generally agreed that a conducting surface state exists, and it appears to be sensitive to magnetic probes such as Gd. The apparent gap protection seen in the measurements carefully separating bulk from surface resistivity remains a mystery. Related to this is that the bulk resistivity follows a simple activation law with no apparent carrier lifetime variation. The high field bulk de Haas – van Alphen oscillations also present mysteries, both as to their occurrence and their similarity to the signals seen in the trivalent, metallic hexaborides. The large ac conductivity is equally puzzling. There are clearly effects extrinsic to the fundamental physics of SmB₆ seen, for example, in the sample dependence of the low temperature specific heat and magnetic susceptibility. The source of the bulk low-temperature

tail in the magnetic susceptibility needs to be identified as well as the bump seen in the specific heat at low temperature. One route to sorting out these puzzles will be a more detailed sample characterization of the crystals actually used in each experiment. Fully understanding the physics of defects appears to be a requisite for understanding this unusual compound. Surely there are other materials to be discovered carrying the same physics, and identifying the common physics can provide another path forward. YbB_{12} seems a possible but not certain candidate, but other examples are highly desired and await discovery.

Acknowledgments

The authors of this chapter acknowledge stimulating discussions with Sean M. Thomas, Joe D. Thompson, Steffen Wirth, Pascoal Pagliuso, Yun Suk Eo, Wesley Fuhrman, Cagliyan Kurdak, James Allen, Liang Fu, Piers Coleman, and Peter Riseborough. Work at Los Alamos was performed under the auspices of the U. S. Department of Energy, Office of Basic Energy Sciences, Division of Materials Science and Engineering.

References

- [1] Schuth, V. and von Stackelberg, M.; "Magneto-chemical investigations. VII. On the magnetism of borides of rare earths."; *Z. Kristallogr. Chem.* **19(5)**, 321–327 (1932).
- [2] Samsonov, G. V., Zhuravlev, N. N., Paderno, Y., and Melik-Adamyanyan, V. R.; "Preparation and properties of Samarium hexaboride"; *Soviet Phys.-and Cryst.* **4** (1960).
- [3] Fisk, Z. and Remeika, J. P.; "Growth of single crystals from molten metal fluxes"; *Handbook on the Physics and Chemistry of Rare Earths* **12**, 53–70 (1989).
- [4] Canfield, P. C. and Fisk, Z.; "Growth of single crystals from metallic fluxes"; *Phil. Mag.* **65**, 1117–1123 (1992).
- [5] Rosa, P. F. S. and Fisk, Z.; "Crystal growth of intermetallics"; *Crystal growth of intermetallics* 49–60 (2018).
- [6] Prokofiev, A.; "Floating zone growth of intermetallic compounds"; *Crystal Growth of Intermetallics* 91–116 (2019).

44 | Chapter 1 Bulk and surface properties of SmB_6

- [7] Phelan, W. A., Koohpayeh, S. M., Cottingham, P., Tutmaher, J. A., Leiner, J. C., Lumsden, M. D., Lavelle, C. M., Wang, X. P., Hoffmann, C., Siegler, M. A., Haldolaarachchige, N., Young, D. P., and McQueen, T. M.; "On the chemistry and physical properties of flux and floating zone grown SmB_6 single crystals"; *Sci. Rep.* **6**, 1–10 (2016).
- [8] Allard, G.; "X-ray study of some borides"; *Bull. Soc. Chim. Fr.* **51**, 1213–1215 (1932).
- [9] Pauling, L. and Weinbaum, S.; "The structure of calcium boride, CaB_6 "; *Z. Kristallogr. Cryst. Mater.* **87**, 181–182 (1934).
- [10] Longuet-Higgins, H. C. and Roberts, M. D.; "The electronic structure of the borides MB_6 "; *Proceedings of the royal society of London Series A - Mathematical and physical sciences* **224**, 336–347 (1954).
- [11] Arko, A. J., Crabtree, G., Karim, D., Mueller, F. M., Windmiller, L. R., Ketterson, J. B., and Fisk, Z.; "de Haas-van Alphen effect and the Fermi surface of LaB_6 "; *Phys. Rev. B* **13**, 5240–5247 (1976).
- [12] Ishizawa, Y., Tanaka, T., Bannai, E., and Kawai, S.; "de Haas-van Alphen effect and Fermi surface of LaB_6 "; *J. Phys. Soc. Jpn.* **42**, 112–118 (1977).
- [13] Onuki, Y., Umezawa, A., Kwok, W. K., Crabtree, G. W., Nishihara, M., Yamazaki, T., Omi, T., and Komatsubara, T.; "High-field magnetoresistance and de Haas-van Alphen effect in antiferromagnetic PrB_6 and NdB_6 "; *Phys. Rev. B* **40**, 11195–11207 (1989).
- [14] Aeppli, G. and Fisk, Z.; "Kondo insulators"; *Comments Cond. Mat. Phys.* **16** (1992).
- [15] Kasaya, M., Tarascon, J., and Etourneau, J.; "Study of the valence transition in La- and Yb-substituted SmB_6 "; *Solid State Comm.* **33**, 1005–1007 (1980).
- [16] Mott, N. F.; "Rare-earth compounds with mixed valencies"; *Phil. Mag.* **30**, 403–416 (1974).
- [17] Martin, R. M. and Allen, J. W.; "Theory of mixed valence: Metals or small gap insulators (invited)"; *J. Appl. Phys.* **50**, 7561 (1979).
- [18] Kasuya, T., Takegahara, K., Fujita, T., Tanaka, T., and Bannai, E.; "Valence fluctuating state in SmB_6 "; *J. Phys. Colloq.* **40**, C5–308–C5–313 (1979).
- [19] Kikoin, K. A. and Mishchenko, A. S.; "Deformable shell description for the phonon spectra of semiconductors with unstable valency"; *J. Phys.: Condens. Mater.* **2**, 6491–6506 (1990).
- [20] Robinson, P. J., Munarriz, J., Valentine, M. E., Granmoe, A., Drichko, N., Chamorro, J. R., Rosa, P. F., McQueen, T. M., and Alexandrova, A. N.; "Dynamical bonding driving mixed valency in a metal boride"; *Angew. Chem.* (2019); to be published.
- [21] Streltsov, V., Konovalova, E., and Paderno, Y.; "Synchrotron electron density probe of strongly correlated electron systems"; *Phys. B* **259-261**, 1155–1156 (1999).

- [22] Dzero, M., Sun, K., Galitski, V., and Coleman, P.; “Topological Kondo insulators”; *Phys. Rev. Lett.* **104**, 106408 (2010).
- [23] Takimoto, T.; “SmB₆ : A promising candidate for a topological insulator”; *J. Phys. Soc. Jpn.* **80**, 123710 (2011).
- [24] Alexandrov, V., Dzero, M., and Coleman, P.; “Cubic topological Kondo insulators”; *Phys. Rev. Lett.* **111**, 226403 (2013).
- [25] Lu, F., Zhao, J., Weng, H., Fang, Z., and Dai, X.; “Correlated topological insulators with mixed valence”; *Phys. Rev. Lett.* **110**, 096401 (2013).
- [26] Batko, I. and Batkova, M.; “SmB₆: Topological insulator or semiconductor with valence-fluctuation induced hopping transport?”; *Solid State Comm.* **196**, 18–23 (2014).
- [27] Baskaran, G.; “Majorana Fermi sea in insulating SmB₆: A proposal and a theory of quantum oscillations in Kondo insulators”; arXiv:1507.03477 (2015).
- [28] Zhang, L., Song, X.-Y., and Wang, F.; “Quantum oscillation in narrow-gap topological insulators”; *Phys. Rev. Lett.* **116**, 046404 (2016).
- [29] Erten, O., Ghaemi, P., and Coleman, P.; “Kondo breakdown and quantum oscillations in SmB₆”; *Phys. Rev. Lett.* **116**, 046403 (2016).
- [30] Knolle, J. and Cooper, N. R.; “Excitons in topological Kondo insulators: Theory of thermodynamic and transport anomalies in SmB₆”; *Phys. Rev. Lett.* **118**, 096604 (2017).
- [31] Erten, O., Chang, P.-Y., Coleman, P., and Tsvetlik, A. M.; “Skyrme insulators at the brink of superconductivity”; *Phys. Rev. Lett.* **119**, 057603 (2017).
- [32] Ram, P. and Kumar, B.; “Theory of quantum oscillations of magnetization in Kondo insulators”; *Phys. Rev. B* **96**, 075115 (2017).
- [33] Chowdhury, D., Sodemann, I., and Senthil, T.; “Mixed-valence insulators with neutral Fermi surfaces”; *Nat. Comm.* **9**, 1766 (2018).
- [34] Shen, H., Zhen, B., and Fu, L.; “Topological band theory for non-Hermitian Hamiltonians”; *Phys. Rev. Lett.* **120**, 146402 (2018).
- [35] Fuhrman, W. T. and Nikolić, P.; “Magnetic impurities in Kondo insulators and the puzzle of samarium hexaboride”; arXiv:1807.00005 (2018).
- [36] Pal, H. K.; “Anomalies in a slightly doped insulator with strong particle-hole asymmetry and a narrow gap: The case of SmB₆”; *Phys. Rev. B* **99**, 045149 (2019).
- [37] Skinner, B.; “Properties of the donor impurity band in mixed valence insulators”; *Phys. Rev. Materials* **3**, 104601 (2019).
- [38] Riseborough, P. S.; “Heavy fermion semiconductors”; *Adv. Phys.* **49**, 257–320 (2000).
- [39] Dzero, M., Xia, J., Galitski, V., and Coleman, P.; “Topological Kondo insulators”; *Annu. Rev. Condens. Matter Phys.* **7**, 249–280 (2016).

46 | Chapter 1 Bulk and surface properties of SmB_6

- [40] Wu, Q. and Sun, L.; “Puzzle maker in SmB_6 : accompany-type valence fluctuation state”; *Rep. Prog. Phys.* **80**, 112501 (2017).
- [41] Menth, A., Buehler, E., and Geballe, T. H.; “Magnetic and semiconducting properties of SmB_6 ”; *Phys. Rev. Lett.* **22**, 295–297 (1969).
- [42] Nickerson, J. C.; White, R. M.; Lee, K. N.; bachmann, R.; Geballe, T. H.; Hull, G. W.; “Physical properties of SmB_6 ”; *Phys. Rev. B* **3**, 2032 (1971).
- [43] Allen, J. W.; Batlogg, B.; Wachter, P.; “Large low-temperature Hall effect and resistivity in mixed-valent SmB_6 ”; *Phys. B* **20**, 4807 (1979).
- [44] Hatnean, M. C., Lees, M. R., Paul, D. M., and Balakrishnan, G.; “Large, high quality single-crystals of the new Topological Kondo Insulator, SmB_6 ”; *Sci. Rep.* **3**, 3071 (2013).
- [45] Kim, D. J., Xia, J., and Fisk, Z.; “Topological surface state in the Kondo insulator samarium hexaboride”; *Nat. Mat.* **13**, 466–470 (2014).
- [46] Wolgast, S., Kurdak, Ç., Sun, K., Allen, J. W., Kim, D. J., and Fisk, Z.; “Low-temperature surface conduction in the Kondo insulator SmB_6 ”; *Phys. Rev. B* **88**, 1–5 (2013).
- [47] Kim, D. J., Thomas, S., Grant, T., Botimer, J., Fisk, Z., and Xia, J.; “Surface Hall effect and nonlocal transport in SmB_6 : Evidence for surface conduction”; *Sci. Rep.* **3**, 1–4 (2013).
- [48] Zhang, X., Butch, N. P., Syers, P., Ziemak, S., Greene, R. L., and Paglione, J.; “Hybridization, inter-ion correlation, and surface states in the Kondo insulator SmB_6 ”; *Phys. Rev. X* **3**, 011011 (2013).
- [49] Syers, P., Kim, D., Fuhrer, M. S., and Paglione, J.; “Tuning bulk and surface conduction in the proposed topological Kondo insulator SmB_6 ”; *Phys. Rev. Lett.* **114**, 1–5 (2015).
- [50] Gabáni, S., Pristáš, G., Takáčová, I., Sluchanko, N., Siemensmeyer, K., Shitsevalova, N., Filipov, V., and Flachbart, K.; “Surface and bulk components of electrical conductivity in (presumably special topological) Kondo insulator SmB_6 at lowest temperatures”; *Solid State Sci.* **47**, 17–20 (2015).
- [51] Batkova, M., Batko, I., Gabáni, S., Gažo, E., Konovalova, E., and Filippov, V.; “Low temperature resistivity studies of SmB_6 : Observation of two-dimensional variable-range hopping conductivity”; *Phys. B* **536**, 200–202 (2018).
- [52] Phelan, W. A., Koohpayeh, S. M., Cottingham, P., Freeland, J. W., Leiner, J. C., Broholm, C. L., and McQueen, T. M.; “Correlation between bulk thermodynamic measurements and the low-temperature-resistance plateau in SmB_6 ”; *Phys. Rev. X* **4**, 1–10 (2014).
- [53] Zhu, Z.-H., Nicolaou, A., Levy, G., Butch, N. P., Syers, P., Wang, X. F., Paglione, J., Sawatzky, G. A., Elfimov, I. S., and Damascelli, A.; “Polarity-driven surface metallicity in SmB_6 ”; *Phys. Rev. Lett.* **111**, 216402 (2013).

- [54] Eo, Y. S., Rakoski, A., Lucien, J., Mihaliiov, D., Kurdak, Ç., Rosa, P. F. S., and Fisk, Z.; “Transport gap in SmB_6 protected against disorder”; *Proc. Natl. Acad. Sci. U.S.A.* **116**, 12638–12641 (2019).
- [55] Wolgast, S., Eo, Y. S., Kurdak, Ç., Kim, D. J., and Fisk, Z.; “Conduction through subsurface cracks in bulk topological insulators”; arXiv:1506.08233 (2015).
- [56] Rakoski, A., Eo, Y. S., Sun, K., and Kurdak, Ç.; “Understanding low-temperature bulk transport in samarium hexaboride without relying on in-gap bulk states”; *Phys. Rev. B* **95**, 195133 (2017).
- [57] Wakeham, N., Wang, Y. Q., Fisk, Z., Ronning, F., and Thompson, J. D.; “Surface state reconstruction in ion-damaged SmB_6 ”; *Phys. Rev. B* **91**, 085107 (2015).
- [58] Wakeham, N., Wen, J., Wang, Y., Fisk, Z., Ronning, F., and Thompson, J.; “The effect of magnetic and non-magnetic ion damage on the surface state in SmB_6 ”; *J. Magn. Magn. Mater* **400**, 62–65 (2016).
- [59] Gabáni, S., Orendáč, M., Pristáš, G., Gažo, E., Diko, P., Piovarči, S., Glushkov, V., Sluchanko, N., Levchenko, A., Shitsevalova, N., and Flachbart, K.; “Transport properties of variously doped SmB_6 ”; *Phil. Mag.* **96**, 3274–3283 (2016).
- [60] Kim, J., Kim, K., Kang, C.-J., Kim, S., Choi, H. C., Kang, J.-S., Denlinger, J. D., and Min, B. I.; “Termination-dependent surface in-gap states in a potential mixed-valent topological insulator: SmB_6 ”; *Phys. Rev. B* **90**, 075131 (2014).
- [61] Sun, Z., Maldonado, A., Paz, W. S., Inosov, D. S., Schnyder, A. P., Palacios, J. J., Shitsevalova, N. Y., Filipov, V. B., and Wahl, P.; “Observation of a well-defined hybridization gap and in-gap states on the SmB_6 (001) surface”; *Phys. Rev. B* **97**, 235107 (2018).
- [62] Matt, C. E., Pirie, H., Soumyanarayanan, A., He, Y., Yee, M. M., Chen, P., Liu, Y., Larson, D. T., Paz, W. S., Palacios, J. J., Hamidian, M. H., and Hoffman, J. E.; “Consistency between ARPES and STM measurements on SmB_6 ”; *Phys. Rev. B* **101**, 085142 (2020).
- [63] Pirie, H., Liu, Y., Soumyanarayanan, A., Chen, P., He, Y., Yee, M. M., Rosa, P. F. S., Thompson, J. D., Kim, D.-J., Fisk, Z., Wang, X., Paglione, J., Morr, D. K., Hamidian, M. H., and Hoffman, J. E.; “Imaging emergent heavy Dirac fermions of a topological Kondo insulator”; *Nat. Phys.* **16**, 52–56 (2020).
- [64] Röbner, S., Jang, T.-H., Kim, D.-J., Tjeng, L. H., Fisk, Z., Steglich, F., and Wirth, S.; “Hybridization gap and Fano resonance in SmB_6 ”; *Proc. Natl. Acad. Sci. U.S.A.* **111**, 4798–4802 (2014).
- [65] Herrmann, H., Hlawenka, P., Siemensmeyer, K., Weschke, E., Sánchez-Barriga, J., Varykhalov, A., Shitsevalova, N. Y., Dukhnenko, A. V., Filipov, V. B., Gabáni, S., Flachbart, K., Rader, O., Sterrer, M., and Rienks, E. D. L.; “A consistent view of the samarium hexaboride terminations to resolve the nature of its surface states”;

48 | Chapter 1 Bulk and surface properties of SmB_6

- arXiv:1810.13380 (2018).
- [66] Ruan, W., Ye, C., Guo, M., Chen, F., Chen, X., Zhang, G.-M., and Wang, Y.; “Emergence of a coherent in-gap state in the SmB_6 Kondo insulator revealed by scanning tunneling spectroscopy”; *Phys. Rev. Lett.* **112**, 136401 (2014).
 - [67] Jiao, L., Rößler, S., Kim, D. J., Tjeng, L. H., Fisk, Z., Steglich, F., and Wirth, S.; “Additional energy scale in SmB_6 at low-temperature”; *Nat. Comm.* **7**, 13762 (2016).
 - [68] Zabolotnyy, V. B., Fürsich, K., Green, R. J., Lutz, P., Treiber, K., Min, C.-H., Dukhnenko, A. V., Shitsevalova, N. Y., Filipov, V. B., Kang, B. Y., Cho, B. K., Sutarto, R., He, F., Reinert, F., Inosov, D. S., and Hinkov, V.; “Chemical and valence reconstruction at the surface of SmB_6 revealed by means of resonant soft x-ray reflectometry”; *Phys. Rev. B* **97**, 205416 (2018).
 - [69] Rößler, S., Jiao, L., Kim, D. J., Seiro, S., Rasim, K., Steglich, F., Tjeng, L. H., Fisk, Z., and Wirth, S.; “Surface and electronic structure of SmB_6 through scanning tunneling microscopy”; *Phil. Mag.* **96**, 3262–3273 (2016).
 - [70] Jiao, L., Rößler, S., Kasinathan, D., Rosa, P. F. S., Guo, C., Yuan, H., Liu, C.-X., Fisk, Z., Steglich, F., and Wirth, S.; “Magnetic and defect probes of the SmB_6 surface state”; *Sci. Adv.* **4**, eaau4886 (2018).
 - [71] Luo, Y., Chen, H., Dai, J., Xu, Z.-a., and Thompson, J. D.; “Heavy surface state in a possible topological Kondo insulator: Magnetothermoelectric transport on the (011) plane of SmB_6 ”; *Phys. Rev. B* **91**, 075130 (2015).
 - [72] Park, W. K., Sun, L., Noddings, A., Kim, D.-J., Fisk, Z., and Greene, L. H.; “Topological surface states interacting with bulk excitations in the Kondo insulator SmB_6 revealed via planar tunneling spectroscopy”; *Proc. Natl. Acad. Sci. U.S.A.* **113**, 6599–6604 (2016).
 - [73] Sun, L., Kim, D.-J., Fisk, Z., and Park, W. K.; “Planar tunneling spectroscopy of the topological Kondo insulator SmB_6 ”; *Phys. Rev. B* **95**, 195129 (2017).
 - [74] Li, G., Xiang, Z., Yu, F., Asaba, T., Lawson, B., Cai, P., Tinsman, C., Berkley, A., Wolgast, S., Eo, Y. S., Kim, D.-J., Kurdak, C., Allen, J. W., Sun, K., Chen, X. H., Wang, Y. Y., Fisk, Z., and Li, L.; “Two-dimensional Fermi surfaces in Kondo insulator SmB_6 ”; *Science* **346**, 1208–1212 (2014).
 - [75] Xiang, Z., Lawson, B., Asaba, T., Tinsman, C., Chen, L., Shang, C., Chen, X. H., and Li, L.; “Bulk rotational symmetry breaking in Kondo insulator SmB_6 ”; *Phys. Rev. X* **7**, 031054 (2017).
 - [76] Thomas, S. M., Ding, X., Ronning, F., Zapf, V., Thompson, J. D., Fisk, Z., Xia, J., and Rosa, P. F. S.; “Quantum oscillations in flux-grown SmB_6 with embedded aluminum”; *Phys. Rev. Lett.* **122**, 166401 (2019).

- [77] Larson, C. O. and Gordon, W. L.; “Low-Field de Haas – van Alphen Study of the Fermi Surface of Aluminum”; *Phys. Rev.* **156**, 703–715 (1967).
- [78] Neupane, M., Alidoust, N., Xu, S.-Y., Kondo, T., Ishida, Y., Kim, D. J., Liu, C., Belopolski, I., Jo, Y. J., Chang, T.-R., Jeng, H.-T., Durakiewicz, T., Balicas, L., Lin, H., Bansil, A., Shin, S., Fisk, Z., and Hasan, M. Z.; “Surface electronic structure of the topological Kondo-insulator candidate correlated electron system SmB_6 ”; *Nat. Comm.* **4**, 2991 (2013).
- [79] Jiang, J., Li, S., Zhang, T., Sun, Z., Chen, F., Ye, Z., Xu, M., Ge, Q., Tan, S., Niu, X., Xia, M., Xie, B., Li, Y., Chen, X., Wen, H., and Feng, D.; “Observation of possible topological in-gap surface states in the Kondo insulator SmB_6 by photoemission”; *Nat. Comm.* **4**, 3010 (2013).
- [80] Xu, N., Biswas, P. K., Dil, J. H., Dhaka, R. S., Landolt, G., Muff, S., Matt, C. E., Shi, X., Plumb, N. C., Radović, M., Pomjakushina, E., Conder, K., Amato, A., Borisenko, S. V., Yu, R., Weng, H.-M., Fang, Z., Dai, X., Mesot, J., Ding, H., and Shi, M.; “Direct observation of the spin texture in SmB_6 as evidence of the topological Kondo insulator”; *Nat. Comm.* **5**, 4566 (2014).
- [81] Ohtsubo, Y., Yamashita, Y., Hagiwara, K., Ideta, S.-i., Tanaka, K., Yukawa, R., Horiba, K., Kumigashira, H., Miyamoto, K., Okuda, T., Hirano, W., Iga, F., and Kimura, S.-i.; “Non-trivial surface states of samarium hexaboride at the (111) surface”; *Nat. Comm.* **10**, 2298 (2019).
- [82] Hlawenka, P., Siemensmeyer, K., Weschke, E., Varykhalov, A., Sánchez-Barriga, J., Shitsevalova, N. Y., Dukhnenko, A. V., Filipov, V. B., Gabáni, S., Flachbart, K., Rader, O., and Rienks, E. D. L.; “Samarium hexaboride is a trivial surface conductor”; *Nat. Comm.* **9**, 517 (2018).
- [83] Denlinger, J. D., Allen, J. W., Kang, J.-S., Sun, K., Min, B.-I., Kim, D.-J., and Fisk, Z.; “ SmB_6 photoemission: past and present”; *JPS Conf. Proc.* **3**, 017038 (2014).
- [84] Allen, J. W.; “Foreword for special issue of philosophical magazine on: topological correlated insulators and SmB_6 ”; *Phil. Mag.* **96**, 3227–3238 (2016).
- [85] Bat’ko, I., Flachbart, K., Miškuf, J., Filipov, V. M., Konovalova, E. S., and Paderno, J. B.; “Electrical resistivity of SmB_6 thin films”; *J. Less Common Met.* **158**, L17–L19 (1990).
- [86] Waldhauser, W., Mitterer, C., Laimer, J., and Störi, H.; “Sputtered thermionic hexaboride coatings”; *Surf. Coat. Technol.* **98**, 1315–1323 (1998).
- [87] Yong, J., Jiang, Y., Usanmaz, D., Curtarolo, S., Zhang, X., Li, L., Pan, X., Shin, J., Takeuchi, I., and Greene, R. L.; “Robust topological

50 | Chapter 1 Bulk and surface properties of SmB₆

- surface state in Kondo insulator SmB₆ thin films"; *Appl. Phys. Lett.* **105**, 222403 (2014).
- [88] Shaviv Petrushevsky, M., Rout, P. K., Levi, G., Kohn, A., and Dagan, Y.; "Signature of surface state coupling in thin films of the topological Kondo insulator SmB₆ from anisotropic magnetoresistance"; *Phys. Rev. B* **95**, 085112 (2017).
- [89] Shishido, H., Yoneda, Y., Yoshida, T., Noguchi, S., and Ishida, T.; "Semi-epitaxial SmB₆ thin films prepared by the molecular beam epitaxy"; *Phys. Procedia* **75**, 405–412 (2015).
- [90] Cen, C., Ma, Y., Wang, Q., and Eom, C.-B.; "Surface magnetism and proximity effects in hexaboride thin films"; *Appl. Phys. Lett.* **110**, 102404 (2017).
- [91] Batkova, M., Batko, I., Stobiecki, F., Szymański, B., Kuświk, P., Macková, A., and Malinský, P.; "Electrical properties of SmB₆ thin films prepared by pulsed laser deposition from a stoichiometric SmB₆ target"; *J. Alloys Compd.* **744**, 821–827 (2018).
- [92] Lee, S., Zhang, X., Liang, Y., Fackler, S. W., Yong, J., Wang, X., Paglione, J., Greene, R. L., and Takeuchi, I.; "Observation of the superconducting proximity effect in the surface state of SmB₆ thin films"; *Phys. Rev. X* **6**, 031031 (2016).
- [93] Yong, J., Jiang, Y., Zhang, X., Shin, J., Takeuchi, I., and Greene, R. L.; "Magnetotransport in nanocrystalline SmB₆ thin films"; *AIP Advances* **5**, 077144 (2015).
- [94] Liu, T., Li, Y., Gu, L., Ding, J., Chang, H., Janantha, P. A. P., Kalinikos, B., Novosad, V., Hoffmann, A., Wu, R., Chien, C. L., and Wu, M.; "Nontrivial nature and penetration depth of topological surface states in SmB₆ thin films"; *Phys. Rev. Lett.* **120**, 207206 (2018).
- [95] Li, Y., Ma, Q., Huang, S. X., and Chien, C. L.; "Thin films of topological Kondo insulator candidate SmB₆ : Strong spin-orbit torque without exclusive surface conduction"; *Sci. Adv.* **4**, eaap8294 (2018).
- [96] Lee, S., Stanev, V., Zhang, X., Stasak, D., Flowers, J., Higgins, J. S., Dai, S., Blum, T., Pan, X., Yakovenko, V. M., Paglione, J., Greene, R. L., Galitski, V., and Takeuchi, I.; "Perfect Andreev reflection due to the Klein paradox in a topological superconducting state"; *Nature* **570**, 344–348 (2019).
- [97] Brewer, J. R., Deo, N., Morris Wang, Y., and Cheung, C. L.; "Lanthanum hexaboride nanoobelisks"; *Chem. Mater.* **19**, 6379–6381 (2007).
- [98] Xu, J., Hou, G., Mori, T., Li, H., Wang, Y., Chang, Y., Luo, Y., Yu, B., Ma, Y., and Zhai, T.; "Excellent field-emission performances of neodymium hexaboride (NdB₆) nanoneedles with ultra-low work functions"; *Adv. Funct. Mater.* **23**, 5038–5048 (2013).
- [99] Zhang, H., Zhang, Q., Tang, J., and Qin, L.-C.; "Single-crystalline LaB₆ nanowires"; *J. Am. Chem. Soc.* **127**, 2862–2863 (2005).

- [100] Xu, J., Zhao, Y., Shi, Z., Zou, C., and Ding, Q.; "Single-crystalline SmB_6 nanowires"; *J. Cryst. Growth* **310**, 3443–3447 (2008).
- [101] Brewer, J. R., Jacobberger, R. M., Diercks, D. R., and Cheung, C. L.; "Rare earth hexaboride nanowires: General synthetic design and analysis using atom probe tomography"; *Chem. Mater.* **23**, 2606–2610 (2011).
- [102] Zhou, Y., Peng, Y., Yin, Y., Zhou, W., Zhou, F., Liu, C., Liu, G., Sun, L., and Tang, D.; "Large-scale synthesis and electrical transport properties of single-crystalline SmB_6 nanowires"; *J. Phys. D: Appl. Phys.* **49**, 265302 (2016).
- [103] Han, W., Qiu, Y., Zhao, Y., Zhang, H., Chen, J., Sun, S., Lan, L., Fan, Q., and Li, Q.; "Low-temperature synthesis and electronic transport of topological insulator SmB_6 nanowires"; *Cryst. Eng. Comm.* **18**, 7934–7939 (2016).
- [104] Lin, Z., Zhou, Y., Kong, L.-J., Tang, D., Lu, H.-Z., Huang, S.-M., Zhu, R., Xu, J., Lin, F., Wang, J., Liao, Z.-M., and Yu, D.; "Interplay between topological surface states and superconductivity in SmB_6/NbN tunnel junctions"; *Phys. Rev. B* **96**, 165408 (2017).
- [105] Gan, H., Ye, B., Zhang, T., Xu, N., He, H., Deng, S., and Liu, F.; "A controllable solid-source CVD route to prepare topological Kondo insulator SmB_6 nanobelt and nanowire arrays with high activation energy"; *Cryst. Growth Des.* **19**, 845–853 (2019).
- [106] Travaglini, G. and Wachter, P.; "Intermediate-valent SmB_6 and the hybridization model: An optical study"; *Phys. Rev. B* **29**, 893–898 (1984).
- [107] Jackson, C. M., Grüner, G., Fisk, Z., and von Molnar, S.; "Microwave conductivity of SmB_6 "; *Phys. Rev. B* **29**, 4786–4788 (1984).
- [108] Kimura, S.-i., Nanba, T., Kunii, S., and Kasuya, T.; "Low-energy optical excitation in rare-earth hexaborides"; *Phys. Rev. B* **50**, 1406–1414 (1994).
- [109] Nanba, T., Ohta, H., Motokawa, M., Kimura, S., Kunii, S., and Kasuya, T.; "Gap state of SmB_6 "; *Phys. B* **186-188**, 440–443 (1993).
- [110] Tytarenko, A., Nakatsukasa, K., Huang, Y. K., Johnston, S., and van Heumen, E.; "From bad metal to Kondo insulator: temperature evolution of the optical properties of SmB_6 "; *New J. Phys.* **18**, 123003 (2016).
- [111] Gorshunov, B., Sluchanko, N., Volkov, A., Dressel, M., Knebel, G., Loidl, A., and Kunii, S.; "Low-energy electrodynamics of SmB_6 "; *Phys. Rev. B* **59**, 1808–1814 (1999).
- [112] Sluchanko, N. E., Ä lushkov, V. V., Gorshunov, B. P., Demishev, S. V., Kondrin, M. V., Pronin, A. A., Volkov, A. A., Savchenko, A. K., Grüner, G., Bruynseraede, Y., Moshchalkov, V. V., and Kunii, S.; "Intragap states in SmB_6 "; *Phys. Rev. B* **61**, 9906–9909 (2000).

52 | Chapter 1 Bulk and surface properties of SmB_6

- [113] Laurita, N. J., Morris, C. M., Koohpayeh, S. M., Rosa, P. F., Phelan, W. A., Fisk, Z., McQueen, T. M., and Armitage, N. P.; "Anomalous three-dimensional bulk ac conduction within the Kondo gap of SmB_6 single crystals"; *Phys. Rev. B* **94**, 1–10 (2016).
- [114] Laurita, N. J., Morris, C. M., Koohpayeh, S. M., Phelan, W. A., McQueen, T. M., and Armitage, N. P.; "Impurities or a neutral Fermi surface? A further examination of the low-energy ac optical conductivity of SmB_6 "; *Phys. B* **536**, 78–84 (2018).
- [115] Schlottmann, P.; "Impurity bands in Kondo insulators"; *Phys. Rev. B* **46**, 998–1004 (1992).
- [116] Riseborough, P. S.; "Collapse of the coherence gap in Kondo semiconductors"; *Phys. Rev. B* **68**, 235213 (2003).
- [117] Helgren, E., Armitage, N. P., and Grüner, G.; "Frequency-dependent conductivity of electron glasses"; *Phys. Rev. B* **69**, 014201 (2004).
- [118] Geballe, T. H.; "Why I haven't retired"; *Annu. Rev. Condens. Matter Phys* **4**, 1–21 (2013).
- [119] Tan, B. S., Hsu, Y.-T., Zeng, B., Hatnean, M. C., Harrison, N., Zhu, Z., Hartstein, M., Kiourlappou, M., Srivastava, A., Johannes, M. D., Murphy, T. P., Park, J.-H., Balicas, L., Lonzarich, G. G., Balakrishnan, G., and Sebastian, S. E.; "Unconventional Fermi surface in an insulating state"; *Science* **349**, 287–290 (2015).
- [120] Shoenberg, D.; "Magnetic oscillations in metals"; (1984).
- [121] Hartstein, M., Toews, W. H., Hsu, Y.-T., Zeng, B., Chen, X., Hatnean, M. C., Zhang, Q. R., Nakamura, S., Padgett, A. S., Rodway-Gant, G., Berk, J., Kingston, M. K., Zhang, G. H., Chan, M. K., Yamashita, S., Sakakibara, T., Takano, Y., Park, J.-H., Balicas, L., Harrison, N., Shitsevalova, N., Balakrishnan, G., Lonzarich, G. G., Hill, R. W., Sutherland, M., and Sebastian, S. E.; "Fermi surface in the absence of a Fermi liquid in the Kondo insulator SmB_6 "; *Nat. Phys.* **14**, 166–172 (2018).
- [122] Xu, Y., Cui, S., Dong, J. K., Zhao, D., Wu, T., Chen, X. H., Sun, K., Yao, H., and Li, S. Y.; "Bulk Fermi surface of charge-neutral excitations in SmB_6 or not: A heat-transport study"; *Phys. Rev. Lett.* **116**, 246403 (2016).
- [123] Flachbart, K., Reiffers, M., Janos, S., Paderno, Y., Lazorenko, V., and Kononova, E.; "Thermal conductivity of SmB_6 "; *J. Less Common Met.* **88**, L11–L14 (1982).
- [124] Boulanger, M.-E., Laliberté, F., Dion, M., Badoux, S., Doiron-Leyraud, N., Phelan, W. A., Koohpayeh, S. M., Fuhrman, W. T., Chamorro, J. R., McQueen, T. M., Wang, X. F., Nakajima, Y., Metz, T., Paglione, J., and Taillefer, L.; "Field-dependent heat transport in the Kondo insulator SmB_6 : Phonons scattered by magnetic impurities"; *Phys. Rev. B* **97**, 245141 (2018).

- [125] Fuhrman, W. T., Chamorro, J. R., Alekseev, P. A., Mignot, J.-M., Keller, T., Rodriguez-Rivera, J. A., Qiu, Y., Nikolić, P., McQueen, T. M., and Broholm, C. L.; “Screened moments and extrinsic in-gap states in samarium hexaboride”; *Nat. Comm.* **9**, 1539 (2018).
- [126] Wakeham, N., Rosa, P. F. S., Wang, Y. Q., Kang, M., Fisk, Z., Ronning, F., and Thompson, J. D.; “Low-temperature conducting state in two candidate topological Kondo insulators: SmB_6 and $\text{Ce}_3\text{Bi}_4\text{Pt}_3$ ”; *Phys. Rev. B* **94**, 035127 (2016).
- [127] Orendáč, M., Gabáni, S., Pristáš, G., Gažo, E., Diko, P., Farkašovský, P., Levchenko, A., Shitsevalova, N., and Flachbart, K.; “Isosbestic points in doped SmB_6 as features of universality and property tuning”; *Phys. Rev. B* **96**, 115101 (2017).
- [128] Flachbart, K., Gabáni, S., Neumaier, K., Paderno, Y., Pavlík, V., Schuberth, E., and Shitsevalova, N.; “Specific heat of SmB_6 at very low temperatures”; *Phys. B* **378-380**, 610–611 (2006).
- [129] Stankiewicz, J., Evangelisti, M., Rosa, P. F. S., Schlottmann, P., and Fisk, Z.; “Physical properties of Sm_xB_6 single crystals”; *Phys. Rev. B* **99**, 045138 (2019).
- [130] Nyhus, P., Cooper, S. L., Fisk, Z., and Sarrao, J.; “Light scattering from gap excitations and bound states in SmB_6 ”; *Phys. Rev. B* **52**, R14308–R14311 (1995).
- [131] Valentine, M. E., Koohpayeh, S., Phelan, W. A., McQueen, T. M., Rosa, P. F. S., Fisk, Z., and Drichko, N.; “Breakdown of the Kondo insulating state in SmB_6 by introducing Sm vacancies”; *Phys. Rev. B* **94**, 075102 (2016).
- [132] Nyhus, P., Cooper, S. L., Fisk, Z., and Sarrao, J.; “Low-energy excitations of the correlation-gap insulator SmB_6 : A light-scattering study”; *Phys. Rev. B* **55**, 12488–12496 (1997).
- [133] Mörke, I., Dvorač, V., and Wachter, P.; “Raman scattering in intermediate valent SmB_6 ”; *Solid State Comm.* **40**, 331–334 (1981).
- [134] Alekseev, P. A., Ivanov, A. S., Dorner, B., Schober, H., Kikoin, K. A., Mishchenko, A. S., Lazukov, V. N., Konovalova, E. S., Paderno, Y. B., Rumyantsev, A. Y., and Sadikov, I. P.; “Lattice dynamics of intermediate valence semiconductor SmB_6 ”; *EPL* **10**, 457–463 (1989).
- [135] Valentine, M. E., Koohpayeh, S., Phelan, W. A., McQueen, T. M., Rosa, P. F., Fisk, Z., and Drichko, N.; “An effect of Sm vacancies on the hybridization gap in topological Kondo insulator candidate SmB_6 ”; *Phys. B* **536**, 60–63 (2018).
- [136] Mizumaki, M., Tsutsui, S., and Iga, F.; “Temperature dependence of Sm valence in SmB_6 studied by X-ray absorption spectroscopy”; *J. Phys.: Conf. Series* **176**, 012034 (2009).
- [137] Cohen, R. L., Eibschütz, M., West, K. W., and Buehler, E.; “Electronic configuration of SmB_6 ”; *J. Appl. Phys.* **41**, 898–899 (1970).

54 | Chapter 1 Bulk and surface properties of SmB_6

- [138] Vainshtein, E. E., Blokhin, S. M., and Paderno, Y. B.; "X-ray spectral investigation of samarium hexaboride"; *Sov Phys Sol State, USSR* **6**, 2318+ (1965).
- [139] Cohen, R. L., Eibschütz, M., and West, K. W.; "Electronic and magnetic structure of SmB_6 "; *Phys. Rev. Lett.* **24**, 383–386 (1970).
- [140] Tarascon, J., Isikawa, Y., Chevalier, B., Etourneau, J., Hagenmuller, P., and Kasaya, M.; "Temperature dependence of the samarium oxidation state in SmB_6 and $\text{Sm}_{1-x}\text{La}_x\text{B}_6$ "; *Journal de Physique* **41**, 1141–1145 (1980).
- [141] Mandrus, D., Sarrao, J. L., Lacerda, A., Migliori, A., Thompson, J. D., and Fisk, Z.; "Low-temperature thermal expansion of SmB_6 : Evidence for a single energy scale in the thermodynamics of Kondo insulators"; *Phys. Rev. B* **49**, 16809–16812 (1994).
- [142] Nakamura, S., Goto, T., Kasaya, M., and Kunii, S.; "Electron-strain interaction in valence-fluctuation compound SmB_6 "; *J. Phys. Soc. Jpn.* **60**, 4311–4318 (1991).
- [143] Allen, J. W., Johansson, L. I., Lindau, I., and Hagstrom, S. B.; "Surface mixed valence in Sm and SmB_6 "; *Phys. Rev. B* **21**, 1335–1343 (1980).
- [144] Hayashi, H., Kanai, N., Kawamura, N., Mizumaki, M., Imura, K., Sato, N. K., Suzuki, H. S., and Iga, F.; "A new method for determining the valence of lanthanide compounds: $L\gamma_4$ emission spectroscopy"; *J. Anal. At. Spectrom.* **28**, 373 (2013).
- [145] Lutz, P., Thees, M., Peixoto, T. R., Kang, B. Y., Cho, B. K., Min, C. H., and Reinert, F.; "Valence characterisation of the subsurface region in SmB_6 "; *Phil. Mag.* **96**, 3307–3321 (2016).
- [146] Utsumi, Y., Kasinathan, D., Ko, K.-T., Agrestini, S., Haverkort, M. W., Wirth, S., Wu, Y.-H., Tsuei, K.-D., Kim, D.-J., Fisk, Z., Tanaka, A., Thalmeier, P., and Tjeng, L. H.; "Bulk and surface electronic properties of SmB_6 : A hard x-ray photoelectron spectroscopy study"; *Phys. Rev. B* **96**, 155130 (2017).
- [147] Tsutsui, S., Masuda, R., Kobayashi, Y., Yoda, Y., Mizuuchi, K., Shimizu, Y., Hidaka, H., Yanagisawa, T., Amitsuka, H., Iga, F., and Seto, M.; "Synchrotron radiation Mössbauer spectroscopy using ^{149}Sm nuclei"; *J. Phys. Soc. Jpn.* **85**, 083704 (2016).
- [148] Derr, J., Knebel, G., Braithwaite, D., Salce, B., Flouquet, J., Flachbart, K., Gabáni, S., and Shitsevalova, N.; "From unconventional insulating behavior towards conventional magnetism in the intermediate-valence compound SmB_6 "; *Phys. Rev. B* **77**, 193107 (2008).
- [149] Cooley, J., Aronson, M., Fisk, Z., and Canfield, P.; "High pressure insulator-metal transition in SmB_6 "; *Phys. B* **199-200**, 486–488 (1994).
- [150] Barla, A., Derr, J., Sanchez, J. P., Salce, B., Lapertot, G., Doyle, B. P., Ruffer, R., Lengsdorf, R., Abd-Elmeguid, M. M., and Flouquet, J.; "High-pressure ground state of SmB_6 : Electronic conduction and

- long range magnetic order"; *Phys. Rev. Lett.* **94**, 166401 (2005).
- [151] Zhou, Y., Rosa, P. F. S., Guo, J., Cai, S., Yu, R., Jiang, S., Yang, K., Li, A., Si, Q., Wu, Q., Fisk, Z., and Sun, L.; "Hall-coefficient diagnostics of the surface state in pressurized SmB_6 "; *Phys. Rev. B* **101**, 125116 (2020).
- [152] Beurepaire, E., Kappler, J. P., and Krill, G.; "X-ray-absorption near-edge structure study in mixed-valent samarium systems"; *Phys. Rev. B* **41**, 6768–6776 (1990).
- [153] Butch, N. P., Paglione, J., Chow, P., Xiao, Y., Marianetti, C. A., Booth, C. H., and Jeffries, J. R.; "Pressure-resistant intermediate valence in the Kondo insulator SmB_6 "; *Phys. Rev. Lett.* **116**, 156401 (2016).
- [154] Zhou, Y., Wu, Q., Rosa, P. F., Yu, R., Guo, J., Yi, W., Zhang, S., Wang, Z., Wang, H., Cai, S., Yang, K., Li, A., Jiang, Z., Zhang, S., Wei, X., Huang, Y., Sun, P., Yang, Y.-f., Fisk, Z., Si, Q., Zhao, Z., and Sun, L.; "Quantum phase transition and destruction of Kondo effect in pressurized SmB_6 "; *Sci. Bull.* **62**, 1439–1444 (2017).
- [155] Chen, K., Weng, T.-C., Schmerber, G., Gurin, V. N., Kappler, J.-P., Kong, Q., Baudelet, F., Polian, A., and Nataf, L.; "Surface- and pressure-induced bulk Kondo breakdown in SmB_6 "; *Phys. Rev. B* **97**, 235153 (2018).
- [156] Emi, N., Kawamura, N., Mizumaki, M., Koyama, T., Ishimatsu, N., Pristáš, G., Kagayama, T., Shimizu, K., Osanai, Y., Iga, F., and Mito, T.; "Kondo-like behavior near the magnetic instability in SmB_6 : Temperature and pressure dependences of the Sm valence"; *Phys. Rev. B* **97**, 161116 (2018).
- [157] Emi, N., Mito, T., Kawamura, N., Mizumaki, M., Ishimatsu, N., Pristáš, G., Kagayama, T., Shimizu, K., Osanai, Y., and Iga, F.; "Temperature and pressure dependences of Sm valence in intermediate valence compound SmB_6 "; *Phys. B* **536**, 197–199 (2018).
- [158] Fuhrman, W. T., Leiner, J. C., Freeland, J. W., van Veenendaal, M., Koohpayeh, S. M., Phelan, W. A., McQueen, T. M., and Broholm, C.; "Magnetic dichroism in the Kondo insulator SmB_6 "; *Phys. Rev. B* **99**, 020401 (2019).
- [159] He, H., Miao, L., Augustin, E., Chiu, J., Wexler, S., Breitweiser, S. A., Kang, B., Cho, B. K., Min, C.-H., Reinert, F., Chuang, Y.-D., Denlinger, J., and Wray, L. A.; "Irreversible proliferation of magnetic moments at cleaved surfaces of the topological Kondo insulator SmB_6 "; *Phys. Rev. B* **95**, 195126 (2017).
- [160] Sundermann, M., Yavaş, H., Chen, K., Kim, D. J., Fisk, Z., Kasinathan, D., Haverkort, M. W., Thalmeier, P., Severing, A., and Tjeng, L. H.; "4f crystal field ground state of the strongly correlated topological insulator SmB_6 "; *Phys. Rev. Lett.* **120**, 016402 (2018).
- [161] Amorese, A., Stockert, O., Kummer, K., Brookes, N. B., Kim, D.-J., Fisk, Z., Haverkort, M. W., Thalmeier, P., Tjeng, L. H., and Severing,

56 | Chapter 1 Bulk and surface properties of SmB_6

- A.; "Resonant inelastic x-ray scattering investigation of the crystal-field splitting of Sm^{3+} in SmB_6 "; *Phys. Rev. B* **100**, 241107 (2019).
- [162] Alekseev, P., Ivanov, A., Lazukov, V., Sadikov, I., and Severing, A.; "Temperature effects in phonon dispersion of SmB_6 intermediate valence semiconductor"; *Phys. B* **180-181**, 281–283 (1992).
- [163] Alekseev, P. A., Lazukov, V. N., Osborn, R., Rainford, B. D., Sadikov, I. P., Konovalova, E. S., and Paderno, Y. B.; "Neutron scattering study of the intermediate-valent ground state in SmB_6 "; *EPL* **23**, 347–353 (1993).
- [164] Alekseev, P. A., Mignot, J. M., Rossat-Mignod, J., Lazukov, V. N., Sadikov, I. P., Konovalova, E. S., and Paderno, Y. B.; "Magnetic excitation spectrum of mixed-valence SmB_6 studied by neutron scattering on a single crystal"; *J. Phys.: Condens. Mater.* **7**, 289–305 (1995).
- [165] Alekseev, P. A., Lazukov, V. N., Nemkovskii, K. S., and Sadikov, I. P.; "Magnetic excitations in systems with a nonmagnetic ground state and valence fluctuations"; *JETP* **111**, 285–291 (2010).
- [166] Fuhrman, W. T., Leiner, J., Nikolić, P., Granroth, G. E., Stone, M. B., Lumsden, M. D., DeBeer-Schmitt, L., Alekseev, P. A., Mignot, J.-M., Koohpayeh, S. M., Cottingham, P., Phelan, W. A., Schoop, L., McQueen, T. M., and Broholm, C.; "Interaction driven subgap spin exciton in the Kondo insulator SmB_6 "; *Phys. Rev. Lett.* **114**, 036401 (2015).
- [167] Peña, O., Lysak, M., MacLaughlin, D., and Fisk, Z.; "Nuclear spin relaxation, hybridization, and low-temperature 4f spin fluctuations in intermediate-valent SmB_6 "; *Solid State Comm.* **40**, 539–541 (1981).
- [168] Bose, M., Roy, K., and Basu, A.; " ^{11}B NMR study of intermediate valent SmB_6 "; *J. Phys. C* **13**, 3951–3959 (1980).
- [169] Takigawa, M., Yasuoka, H., Kitaoka, Y., Tanaka, T., Nozaki, H., and Ishizawa, Y.; "NMR study of a valence fluctuating compound SmB_6 "; *J. Phys. Soc. Jpn.* **50**, 2525–2532 (1981).
- [170] Peña, O., MacLaughlin, D. E., Lysak, M., and Fisk, Z.; "NMR and spin/charge fluctuations in intermediate-valent SmB_6 "; *J. Appl. Phys.* **52**, 2152–2154 (1981).
- [171] Caldwell, T., Reyes, A. P., Moulton, W. G., Kuhns, P. L., Hoch, M. J. R., Schlottmann, P., and Fisk, Z.; "High-field suppression of in-gap states in the Kondo insulator SmB_6 "; *Phys. Rev. B* **75**, 075106 (2007).
- [172] Schlottmann, P.; "NMR relaxation in the topological Kondo insulator SmB_6 "; *Phys. Rev. B* **90**, 165127 (2014).
- [173] Pristáš, G., Mito, T., Kohara, T., Gabáni, S., Reiffers, M., Flachbart, K., Takeshita, N., and Shitsevalova, N.; " ^{11}B -NMR study of SmB_6 under pressure"; *Acta Physica Polonica A* **118**, 895–896 (2010).
- [174] Pristáš, G., Mito, T., Kohara, T., Gabáni, S., Reiffers, M., Flachbart, K., Takeshita, N., and Shitsevalova, N.; "Pressure-induced suppression

- of energy gap in the Kondo insulator SmB_6 studied by $^{11}\text{B-NMR}$ "; *J. Phys. Soc. Jpn.* **80**, SA078 (2011).
- [175] Nishiyama, K., Mito, T., Ueda, K.-i., Koyama, T., Kohara, T., Pristáš, G., Gabáni, S., Reiffers, M., Flachbart, K., Komaki, Y., Kokubu, M., Fukazawa, H., Kohori, Y., Takeshita, N., and Shitsevalova, N.; "Effect of pressure on the intermediate-valence semiconductor SmB_6 : $^{11}\text{B-NMR}$ "; *J. Korean Phys. Soc.* **62**, 2024–2027 (2013).
- [176] Biswas, P. K., Salman, Z., Neupert, T., Morenzoni, E., Pomjakushina, E., von Rohr, F., Conder, K., Balakrishnan, G., Hatnean, M. C., Lees, M. R., Paul, D. M., Schilling, A., Baines, C., Luetkens, H., Khasanov, R., and Amato, A.; "Low-temperature magnetic fluctuations in the Kondo insulator SmB_6 "; *Phys. Rev. B* **89**, 161107 (2014).
- [177] Gheidi, S., Akintola, K., Akella, K. S., Côté, A. M., Dunsiger, S. R., Broholm, C., Fuhrman, W. T., Saha, S. R., Paglione, J., and Sonier, J. E.; "Intrinsic low-temperature magnetism in SmB_6 "; *Phys. Rev. Lett.* **123**, 197203 (2019).
- [178] Biswas, P. K., Legner, M., Balakrishnan, G., Hatnean, M. C., Lees, M. R., Paul, D. M., Pomjakushina, E., Prokscha, T., Suter, A., Neupert, T., and Salman, Z.; "Suppression of magnetic excitations near the surface of the topological Kondo insulator SmB_6 "; *Phys. Rev. B* **95**, 020410 (2017).
- [179] Akintola, K., Pal, A., Potma, M., Saha, S. R., Wang, X. F., Paglione, J., and Sonier, J. E.; "Quantum spin fluctuations in the bulk insulating state of pure and Fe-doped SmB_6 "; *Phys. Rev. B* **95**, 245107 (2017).
- [180] Akintola, K., Pal, A., Dunsiger, S. R., Fang, A. C. Y., Potma, M., Saha, S. R., Wang, X., Paglione, J., and Sonier, J. E.; "Freezing out of a low-energy bulk spin exciton in SmB_6 "; *npj Quantum Mater.* **3**, 36 (2018).
- [181] Rupp, L. and Schmidt, P.; "Conduction-electron spin resonance in alkaline-earth hexaborides"; *J. Phys. Chem. Solids* **30**, 1059–1062 (1969).
- [182] Sturm, H., Elschner, B., and Höck, K. H.; "ESR Spectra of Er^{3+} in SmB_6 "; *Phys. Rev. Lett.* **54**, 1291–1294 (1985).
- [183] Weber, C., Sigmund, E., and Wagner, M.; "Distorted $4f-5d$ hybridization as a Jahn-Teller phenomenon"; *Phys. Rev. Lett.* **55**, 1645–1648 (1985).
- [184] Lesseux, G. G., Rosa, P. F. S., Fisk, Z., Schlottmann, P., Pagliuso, P. G., Urbano, R. R., and Rettori, C.; "Anharmonic rattling vibrations effects in the ESR of Er^{3+} doped SmB_6 Kondo insulator"; *AIP Advances* **7**, 055709 (2017).
- [185] Wiese, G., Schäffer, H., and Elschner, B.; "Possible $4f^7 5d^1$ ground state of Gd impurities in the mixed-valence compound SmB_6 , observed with electron spin resonance"; *EPL* **11**, 791–796 (1990).

58 | Chapter 1 Bulk and surface properties of SmB₆

- [186] Souza, J. C., Rosa, P. F. S., Wirth, S., König, M., Lesseux, G. G., Urbano, R. R., Fisk, Z., Pagliuso, P. G., and Sichelschmidt, J.; "Revisiting the possible $4f^7 5d^1$ ground state of Gd impurities in SmB₆ by electron spin resonance"; *JPS Conf. Proc.* **30**, 011021 (2020).